Measurements and Computation of Low Mass Transfer Coefficients for FCC Particles with Ozone Decomposition Reaction

Mayank Kashyap and Dimitri Gidaspow
Dept. of Chemical and Biological Engineering, Illinois Institute of Technology, Chicago, IL 60616

DOI 10.1002/aic.12615
Published online May 2, 2011 in Wiley Online Library (wileyonlinelibrary.com).

The mass transfer coefficients and Sherwood numbers for catalyzed fluid cracking catalyst particles were measured and computed in a two-dimensional (2-D) bubbling fluidized bed, with ozone decomposition reaction. The measured and computed Sherwood numbers, using 3- and 2-D kinetic theory based computational fluid dynamics simulations, were of the order of 10^{-6}–10^{-2}. The low Sherwood numbers were in reasonable agreement with the literature data for small particles, at low Reynolds numbers. The computational fluid dynamics simulations showed that it is possible to compute conversions in fluidized bed reactors without using the conventional model with empirical mass transfer coefficients. © 2011 American Institute of Chemical Engineers *AIChE J,* 58: 707–729, 2012

Keywords: fluidization, computational fluid dynamics, kinetic theory, Sherwood number, clusters and bubbles, core-annular regime

Introduction

The conventional design of fluidized bed reactor requires the knowledge of dispersion and mass transfer coefficients. Gunn[1] and Kato et al.[2] showed that the Sherwood number for large particles is equal to the diffusion limit of two plus the convection conveyed in terms of the Reynolds and Schmidt numbers. However, the Sherwood numbers for fine particles are known to be much smaller than those for large particles.[3–5] Breault[6] and Breault and Guenther[7] reviewed that the Sherwood number varies by at least seven orders of magnitude in the literature, i.e., from 10^{-5} to 10^{2}. The Sherwood numbers for small particles are low due to the formation of clusters,[8] which increases the mass transfer resistance due to restricted movement of gas into dense clusters. In addition, as explained by Chalermsinsuwan et al.,[5] the conventional definition of Sherwood number in fluidized beds utilizes only the difference between the radial distribution of concentration caused by hydrodynamics, and not by diffusional resistance between bulk and particle surface. In view of the fact that the Sherwood number is directly related to the particle size, the formation of cluster in the system does not necessarily mean low mass transfer.

This study presents the measurements and computation of mass transfer coefficients and Sherwood numbers, with decomposition of ozone on the surface of catalyzed fluid cracking catalyst (FCC) particles, in a two-dimensional (2-D) bubbling fluidized bed at IIT, using the concept of additive diffusional and chemical reaction resistances. The reaction rate constants were measured in the free board region by utilizing the ozone and solids concentrations. The measurements, and 3- and 2-D kinetic theory based computational fluid dynamics (CFD) simulations using FLUENT, showed variations in Sherwood number by four orders of magnitude, i.e., from 10^{-6} to 10^{-2}. The mass transfer coefficients varied by three orders of magnitude, i.e., from 10^{-6} to 10^{-3} m/s. Here, the Sherwood numbers were within the literature values at low Reynolds numbers.[6,7] The mass transfer coefficients and Sherwood numbers vary significantly in the

Correspondence concerning this article should be addressed to M. Kashyap at kashmay@iit.edu.

literature due to different flow regimes and locations of data acquisition in fluidized beds. In this study, the Sherwood number increased by three orders of magnitude by replacing the particle size with the cluster or bubble size in the Sherwood number equation for particles.

Ozone Decomposition Reaction

Among other reactions, the ozone decomposition reaction has been utilized by various authors[4,5,9–19] as the chemical reaction for studying reactions in fluidized beds. A recent publication (Kashyap and Gidaspow[20]) described the use of ozone decomposition reaction in two different fluidized bed systems. It has been shown in the literature (Frye et al.,[21] Fryer and Potter,[9] Jiang et al.,[22] Pagliolico et al.,[23] Ouyang et al.,[10,11] and Hansen et al.[15]) that the ozone decomposition reaction is a simple irreversible first order catalytic reaction, given as:

$$2O_{3(g)} \rightarrow 3O_{2(g)} \tag{1}$$

where, 2 mols of ozone gas are converted to 3 mols of oxygen gas. The rate of reaction for ozone decomposition can be written as:

$$\text{Rate of ozone decompostion reaction} = r_{O_3} = -k_{\text{reaction}} C_{O_3} \varepsilon_s \tag{2}$$

where, r_{O_3} is the rate of reaction; k_{reaction} is the reaction rate constant; C_{O_3} is the ozone concentration; ε_s is the solids volume fraction of catalyst.

As shown by Chalermsinsuwan et al.,[5] the total or effective resistance can be shown as the sum of reaction and mass transfer resistances for the first order reaction. In view of the facts that very low concentrations of ozone are sufficient to carry out the ozone decomposition reaction; the production of heat is low during the reaction; the reaction can take place at room temperatures; it is easy to perform the experiments; the ozone concentrations can be measured fast and accurately using ozone analyzers,[13] the ozone decomposition reaction was selected in this study for the measurements and computation of mass transfer coefficients in the riser section of the IIT 2-D circulating fluidized bed (CFB).

Differential Reactor System

The ozone decomposition reaction on the surface of catalyzed 76 μm FCC particles was utilized for the measurements of mass transfer coefficients in the riser section of the 2-D CFB at IIT. Figure 1 shows the schematic diagram of the IIT 2-D CFB. The interior walls of the riser section of the CFB were made up of 0.013 m thick glass sheets to avoid sticking of FCC particles to the walls due to electrostatics caused by abrasion. The fluidized bed had the inside dimensions of 0.305 m width (radial- or x-axis) by 1.283 m height (axial- or y-axis) by 0.051 m depth (tangential- or z-axis). The glass structure of the riser section of the CFB was enclosed within a 0.013 m thick acrylic sheet framework. The downcomer section of the CFB was made up of 0.013 m thick acrylic sheets, with the inside dimensions as 0.305 m width by 1.397 m height by 0.051 m depth. To support

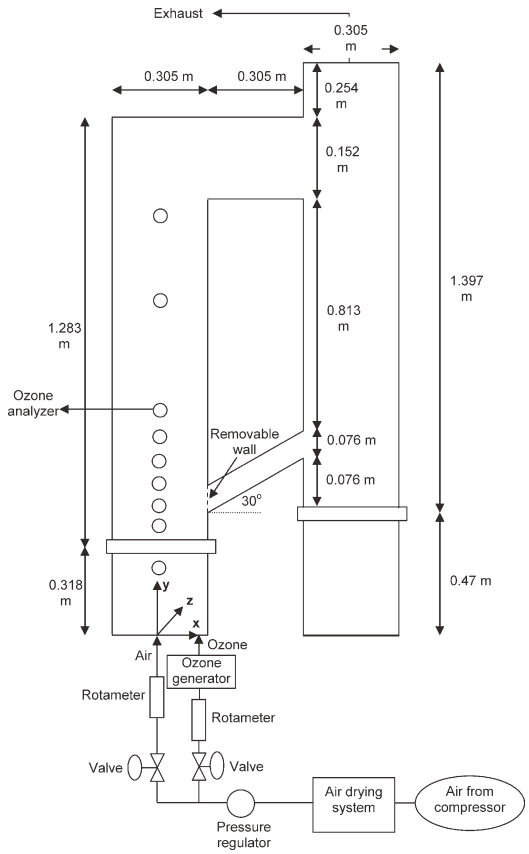

Figure 1. Schematic diagram of the IIT 2-D CFB, modified for the measurements of mass transfer coefficients, with ozone decomposition reaction.

the bed of FCC particles, fine 304 L stainless steel wire support grids (165 × 1400 mesh) were placed at the bases of the riser and downcomer sections of the CFB. In order to attain uniform distribution of air at the inlets of the fluidized bed, two 0.318 m and 0.47 m tall gas distributors were placed below the support grids in the riser and downcomer sections, respectively. The riser and downcomer sections were 0.305 m apart, and were connected by an acrylic cuboid connector with openings of 0.076 m on each side, placed at an angle of 30 degrees with the horizontal, at 0.076 m above the distributors. The top sections of the riser and downcomer were connected by an acrylic cuboid connector with openings of 0.152 m height on each side.

The compressed air used as the fluidizing gas was conditioned before entering the riser section of the 2-D CFB. In the first attempt to dry moisture from the air, a heating coil was used around the inlet gas pipe. Then, the remaining water was removed from the air stream by flowing air through a silica gel bed, before entering another water filter installed in the pipe line. Next, a pressure regulator was used to keep the air pressure constant at 30 psig.

Thereafter, the air flow rate into the riser section of the 2-D CFB was controlled by directing the air stream through a rotameter with a manual valve. The air entered the distributor axially (y-axis) at the bottom, and radially (x-axis) and tangentially (z-axis) at the center. In a parallel pipeline beyond the pressure regulator, the ozone into the riser section of the 2-D

CFB was generator in the ozone generator installed after a barbed ball valve followed by a rotameter with the capability to measure extremely low flow rates of air. The ozone entered the distributor axially at the bottom, radially (x-axis) very close to the entrance for the fluidizing air, and tangentially (z-axis) at the center. Air from the top of the downcomer section of the CFB was discharged to atmosphere through an exhaust pipe. The downcomer section of the CFB was separated from the riser section with the use of a temporary removable wall to fluidize the particles in the bubbling fluidization regime.

The fluidized bed was used as a differential reactor, with eight holes fitted with PVC barbed ball valves, radially (x-axis) at the center and tangentially (z-axis) on the front wall, along the axial (y-axis) direction. The valves were fitted by cautiously self-drilling the glass and acrylic walls, using a drill bit for glass. The purpose of installing the valves was to withdraw time series samples of the mixture of ozone and air for further analysis by the ozone analyzer. Small Teflon tubes were connected to the inside openings of each barbed ball valve to withdraw gas samples tangentially (z-axis) from the center of the fluidized bed. Two more PVC barbed ball valves were fitted on the distributor and at the top of the riser section to analyze the ozone concentrations at the inlet and outlet, respectively. Figure 2 shows the photograph of the bottom portion of the riser section of the IIT 2-D CFB system, with the barbed ball valves.

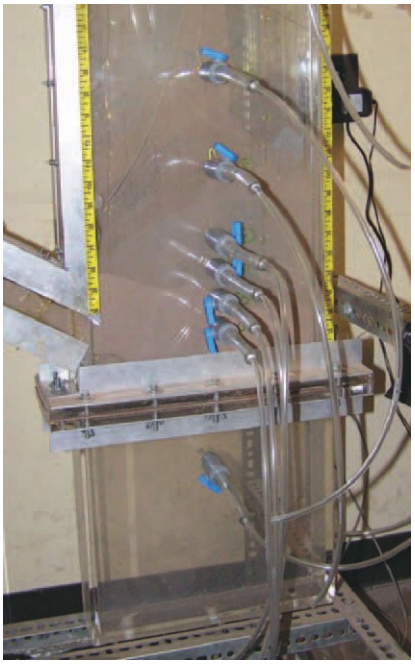

Figure 2. Photograph of the bottom portion of the riser section of the IIT 2-D CFB system for the measurements of ozone concentrations.

[Color figure can be viewed in the online issue, which is available at wileyonlinelibrary.com.]

Apparatuses for the Ozone Decomposition Reaction

Ozone generator

After intensive survey, the ozone generator and the ozone analyzer were obtained from Ozone Solutions. The ozone generator (HG-1500), with variable output control, had a capacity to generate a maximum 750 mg/h ozone on dry air, and 1500 mg/h ozone on oxygen. The gas used in this study was dry air. The ozone generator had 0.0064 m barbed air inlet and ozone outlet connectors. Among the main methods for the production of ozone, i.e., corona discharge, ultraviolet (UV), cold plasma, etc., the corona discharge method was the principle for the generation of ozone in this system. The corona discharge ozone generator was operated fundamentally by passing dried oxygen through an electrical field. The electrical current caused the splitting of the oxygen molecules. The oxygen atom then combined with the oxygen molecule to produce ozone. The center of the corona discharge ozone generator system had a dielectric. The electrical charge was diffused over the dielectric surface, thus, creating an electrical field, or corona.

Thermometer and hygrometer

The relative humidity and temperature of the gas mixture in the fluidized bed were measured with standard digital hygrometer and thermometer, respectively.

Ozone analyzer

The ozone analyzer (UV-100), which was a lightweight bench-top UV ozone analyzer, was used to measure the ozone concentrations at the inlet, outlet and eight other positions along the axial direction (y-axis) in the fluidized bed. The analyzer was a product of Eco Sensors. The ozone analyzer setup comprised the ozone analyzer, PVC barbed ball valves with barb connectors to control the flow of the ozone gas at various positions in the fluidized bed to the ozone analyzer, and the Teflon tubes connecting the ozone analyzer and the PVC barbed ball valves. The ozone analyzer had a measuring range of 0.01 to 900 ppm, with a resolution of 0.01 ppm. The response time of the apparatus was 10 s. The ozone concentration output was displayed on an LCD screen. The UV source in the ozone analyzer was a 254 nm mercury lamp. A 30 μm opening screen was placed in the Teflon tube connecting the barbed valves attached to the fluidized bed and the ozone analyzer, to avoid particles from going into the analyzer.

Theory of operation of ozone analyzer

The ozone molecules have maximum absorption by UV light at 254 nm, same as the principal emission wavelength of a low-pressure mercury lamp. The ozone concentration was measured by the ozone analyzer using the Beer's law. The ozone analyzer could measure 0–100 ppm ozone with 2% accuracy, and 100–900 ppm ozone with 5% accuracy. The ozone analyzer was rented precalibrated from Eco Sensors, based on NIST standards. The analyzer was calibrated again at IIT by measuring a known concentration of ozone generated by the ozone generated, when passed through the fluidized bed without particles. The experimental data were transferred to a Dell PC using a USB cable and drivers provided with the ozone analyzer, for further analysis.

Table 1. System Geometry and Properties for the Measurements of Ozone Concentrations in the IIT 2-D CFB

Geometry/Property	Case A	Case B	Case C	Unit
2-D CFB material		Acrylic/glass		–
Riser section width ($D_{2\text{-D}}$)		0.3048		m
Riser section height (H)		1.283		m
Riser section depth ($W_{2\text{-D}}$)		0.051		
Measuring axial distance from the bottom of riser section ($H_{\text{measurement}}$)	$H_0 = 0$, $H_3 = 0.146$, $H_4 = 0.184$, $H_5 = 0.267$, $H_6 = 0.381$, $H_7 = 0.711$, $H_8 = 1.086$	$H_0 = 0$, $H_3 = 0.146$, $H_4 = 0.184$, $H_5 = 0.267$, $H_6 = 0.381$, $H_7 = 0.711$, $H_8 = 1.086$	$H_0 = 0$, $H_1 = 0.076$, $H_2 = 0.108$, $H_3 = 0.146$, $H_4 = 0.184$, $H_5 = 0.267$, $H_6 = 0.381$, $H_7 = 0.711$, $H_8 = 1.086$	m
Measuring horizontal distance from right wall of riser, $X_{\text{measurement}}$ (See Figure 1)		0.152 (Center)		m
Measuring distance from the plane, $z = 0$, $Z_{\text{measurement}}$ (See Figure 1)		0 (Center)		m
Downcomer section width ($D_{\text{downcomer}}$)		0.305		m
Cuboid connector opening ($D_{\text{conecting pipe}}$)		0.076		m
Cuboid connector angle with horizontal ($\alpha_{\text{horizontal}}$)		30		degree
Riser section outlet size (D_{outlet})		0.152		m
Particle type		FCC		–
Particle diameter (d_p)		76		μm
Particle density (ρ_s)		1654		kg/m^3
Packing fraction ($\varepsilon_{s,max}$)		0.66		–
Fluidizing gas		Air		–
Operating temperature (T_g)		298		K
Gas density (ρ_g)		1.2		kg/m^3
Gas viscosity (μ_g)		1.8 x 10^{-5}		kg/(m-s)
Terminal velocity (U_t)		0.28		m/s
Minimum fluidization velocity (U_{mf})		0.003		m/s
Superficial gas velocities (U_g)	0.343	0.337	0.289	m/s
Inlet ozone concentration ($C_{O_3(\text{inlet})}$)	13.2	12.5	10.5	PPM
Initial bed height (H_{initial})		0.054		m
Steady state for time averaging (t_{steady})		60		s

Preparation of Catalyst

The noble metals and transition metal oxides are the active catalysts for the ozone decomposition reaction.[24] In view of the high cost of noble metals, the metal oxide catalysts are usually used for ozone decomposition reactions. The order of the performance of catalysts was shown by Dhandapani and Oyama[24] as follows:

$$MnO_2 > Co_3O_4 > NiO > Fe_2O_3 > Ag_2O > Cr_2O_3 > CeO_2 > MgO > V_2O_5 > CuO$$

The literature survey showed that many types of catalysts can be used for the ozone decomposition reaction. Some of the catalysts used by the previous researchers were: sand particles, impregnated with ferric oxide;[9] FCC particles, impregnated with ferric oxide;[22] γ-alumina particles, impregnated with ferric oxide;[23] and FCC particles, coated with ferric nitrate.[10,11,16]

The FCC particles, impregnated with ferric nitrate, were used as catalysts in this study. The FCC particles, which are primarily composed of porous amorphous aluminum hydrosilicate, were activated by soaking in a 5 wt % solution of ferric nitrate (Sigma-Aldrich), overnight. The FCC particles were then dried and calcined in an oven with a hood at 475°C for 2–3 hours, until no NO_2 was released from ferric nitrate. During this process, the ferric nitrate was converted to ferric oxide, which was the active component for the ozone decomposition reaction:

$$Fe(NO_3)_3.nH_2O \xrightarrow{475^\circ C} \frac{1}{2}Fe_2O_3 + 3NO_2 + \frac{3}{4}O_2 + nH_2O$$

System Properties

Three cases, i.e., Cases A, B and C, of experiments were performed for the measurements of ozone concentrations, with the system geometry and properties described in Table 1. The particles used for the measurements of mass transfer coefficients in the riser section of the IIT 2-D CFB were Geldart A type[25] 76 μm FCC particles, with a particle density of 1654 kg/m^3. The CFB was operated as a bubbling fluidized bed. Dry air was used as the fluidizing gas at room temperature. The inlet ozone gas was mixed with air in the distributor placed at the bottom of the fluidized bed. The concentrations of ozone were measured using the ozone analyzer at various axial levels (y-axis) ranging from 0 to 1.086 m in different cases, where 0 m was the inlet. The ozone concentrations were measured radially (x-axis) at $r/R = 0$ (center), and tangentially (z-axis) at $z/Z = 0$ (center). The solids volume fractions were measured using the light diode assembly: at the axial positions of the measurements of ozone concentrations, radially at the center ($r/R = 0$) and tangentially averaged ($-1 \leq z/Z \leq 1$). The tangentially averaged solids volume fractions were assumed to be equal to those tangentially at the center ($z/Z = 0$).

The experiments for Cases A, B and C were performed with air entering the fluidized bed, from the bottom at

superficial gas velocities of 0.343, 0.337, and 0.289 m/s, respectively. The inlet ozone concentrations for Cases A, B and C were 13.2, 12.5, and 10.5 ppm, respectively. The initial bed height in all the three cases was 0.054 m. The ozone concentration data were averaged over 60 s in each case.

Experimental Procedure for the Measurements of Mass Transfer Coefficients

Ozone concentration measurements

The ozone analyzer was warmed up for about an hour before performing the experiments. A weighed sample of FCC particles, impregnated with ferric oxide, was added to the riser section of the 2-D CFB, and the initial height of the bed was noted. Since the downcomer side of the CFB was blocked with a removable wall, the system was operated as a bubbling fluidized bed. The air flow rate was set to fluidize the particles in the bubbling fluidization regime. The flow rates of air and ozone entering the fluidized bed system were controlled by two previously calibrated rotameters. One rotameter was used to control the fluidizing gas, whereas, the other was used to introduce low amounts of air to the ozone generator. The ozone generator converted the oxygen from air to ozone. The ozone gas and fluidizing air were then mixed in the distributor of the fluidized bed. The concentration of ozone in the fluidizing air into the fluidized bed from the bottom was measured and kept constant throughout the experiment at that particular flow rate of air. The inlet ozone concentration was measured by taking samples of the mixture of air and ozone from the distributor, by opening the PVC barbed ball valve connected to the ozone analyzer. The initial ozone concentrations were fixed at 13.2, 12.5, and 10.5 ppm for experiments in Cases A, B and C, respectively. The heat produced by the chemical reaction was neglected due to low concentrations of ozone in the system.

The expanded bed height was noted visually. To measure the ozone concentrations at different levels along the axial direction (y-axis) in the bubbling fluidized bed, each one of the eight PVC ball valves drilled through the wall of the fluidized bed was opened individually. The samples of the mixture of air and ozone gases were withdrawn from the fluidized bed at various axial positions by moving up from the bottom, each time for 60 s under steady state conditions, for analysis by the ozone analyzer.

Light diode assembly for the measurements of solids volume fractions

A light diode assembly has been used several times to understand the dynamics in fluidized beds by measuring solids volume fractions (Refs. 26–29). The solids volume fractions in this study were measured by recording the voltage generated from a photovoltaic sensor upon passing a constant monochromatic light source through the walls of the fluidized bed. Fiber-Lite A3200 (Dolan-Jenner Industries), with a 200 W bulb, was utilized as the high intensity optical fiber light source. The light source provided an unvarying color uniform light with modulated intensity control. The intensity of light was measured using a high-speed borosilicate detector (Edmunds Optics model NT55-338 15 mm^2). The voltage generated by the detector was inversely proportional to the solids volume fraction. The voltage signal was collected using a National Instruments data collection system, and analyzed using the LabView software.

The Beer-Lambert-Bouguer or Beer's law was the mathematical basis for the light diode assembly technique used to analyze the experimental data for the measurements of solids volume fractions. This technique was in accordance with the concept that the transmitted light can be described as a linear function of the porosity of the system. According to the Beer's law, the intensity of the transmitted light was given as:

$$I = I_0 e^{-\delta \rho l} \tag{6}$$

where, I was the intensity of the transmitted light; I_o was the intensity of incident light; δ was the attenuation coefficient; ρ was the density of the material; l was the path length.

This method utilized the fact that the absorptions for light were different for the gas and solid phases. The solids volume fractions were obtained from the natural logarithm of intensities. From Seo and Gidaspow,[30] the relation between the intensity and the solids volume fractions could be given as:

$$-\ln\left(\frac{I}{I_0}\right) = (A_s - A_g)\,\varepsilon_s + A_g \tag{7}$$

where, $A_s = \delta_s \rho_s l_s$; $A_g = \delta_g \rho_g l_g$.

The coefficients in Eq. 7 were obtained by measuring the light intensities at known solids volume fractions, i.e., from calibration curve obtained by recording voltage outputs through empty ($\varepsilon_s = 0$) and full pipes ($\varepsilon_s = \varepsilon_{s,max}$). The maximum solids volume fraction or the packing fraction, $\varepsilon_s = \varepsilon_{s,max}$, was measured separately, in a static bed as:

$$\varepsilon_{s,\,max.} = \frac{\text{Volume of particles}}{\text{Volume of bed}} = \frac{\left(m_{particles}/\rho_s\right)}{V_{bed}} = \frac{\left(m_{particles}/\rho_s\right)}{\left(D_{2-D}.W_{2-D}.h_{bed}\right)} \approx 0.66 \tag{8}$$

where, $\varepsilon_{s,max}$ was the packing fraction of particles; $m_{particles}$ was the mass of bed of particles (3.73 kg); $D_{2\,-\,D}$ was the inner width of the riser (0.3048 m); $W_{2\,-\,D}$ was the inner depth of the riser (0.051 m); h_{bed} was the height of particles in the static bed (0.22 m); V_{bed} was the volume of bed (0.003 m^3).

The solids volume fractions were measured at different axial positions in the fluidized bed using the light diode assembly. Three sets of data were obtained for calibration, each for the empty pipe and the pipe completely filled with particles, each time for 20 s. Voltages obtained in each set were averaged over the entire time for which the experiments were performed, which were further averaged over all the three sets. After obtaining the coefficients in Eq. 7 using this calibration method, a relation between the voltage output and solids volume fraction was used to measure time dependency of solids volume fraction, for each test run.

Results and Discussion

Ozone concentration

Figure 3 shows the axial variations of the ozone concentrations in the riser section of the CFB reactor operated as

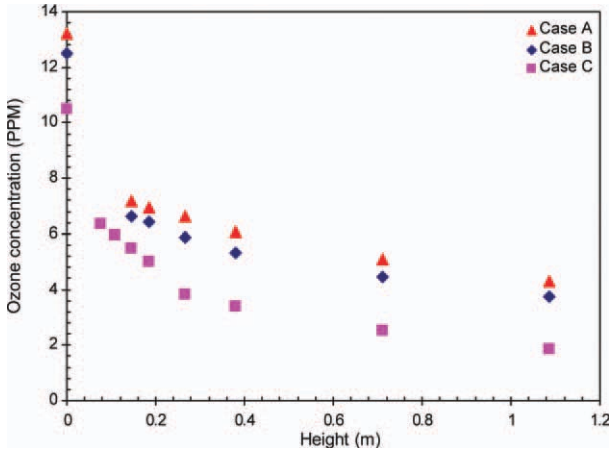

Figure 3. Axial profiles of measured local ozone concentrations, for Cases A, B, and C.

[Color figure can be viewed in the online issue, which is available at wileyonlinelibrary.com.]

bubbling fluidized bed, at three different superficial gas velocities. The concentration of ozone decreased upon moving up in the reactor in all the three cases due to successive conversion caused by reaction on the surface of the catalyst. Ozone was not completely reacted inside the reactor due to partial bypassing of ozone in the center of the fluidized bed, along the tangentially (z-axis) inward direction, and also due to the shallow bed used in this study. This was further due to lower concentration of catalyst at the center than near the walls,[4,5,10,11] in the core-annular regime.[29] In addition, the decrease in the concentration of ozone was more significant at the lowest superficial gas velocity, in Case C, as compared to that at the highest superficial gas velocity, in Case A. This was due to the fact that in the former case, the gas had more time to react on the surface of the catalyst than in the later case.

Solids volume fraction

Figure 4 shows the axial variations of the measured solids volume fractions at three superficial gas velocities, using the light diode assembly. The solids volume fractions varied between 0.2 and 1% at the top of the bubbling bed when the superficial gas velocity was varied between 0.289 and 0.343 m/s. The solids concentrations were close to the packing fraction in the bottom section of the fluidized bed.

Calculation of Mass Transfer Coefficient and Sherwood Number

The principal information needed for understanding a chemical reaction is the reaction rate constant. The experimentally obtained reaction rate constants for the first order ozone decomposition reaction vary by three orders of magnitude in the literature. Chalermsinsuwan et al.[5] recently used four different reaction rate constants by varying them in the range of the values obtained from the literature. In this study, the rates of reaction were obtained from ozone concentrations and solids volume fractions in the bubbling fluidized bed.

The conservation of species equation was written as:

$$\frac{\partial}{\partial t}\left(\varepsilon_g \rho_g y_i\right) + \nabla \cdot \left(\varepsilon_g \rho_g v_g y_i\right) = r_i \tag{9}$$

where, t was the time; ε_g was the voidage; v_g was the actual gas velocity; y_i was the mass fraction of specie, i; r_i was the rate of reaction of specie, i.

The conservation of species equation for ozone, upon integration of Eq. 9 over time and over the radial (x-axis) and tangential (z-axis) directions, gave the 1-D steady state balance as[5,20]:

$$v_y \varepsilon_g \frac{dC_{O_3}}{dY} = r_i \tag{10}$$

where, v_y was the velocity of gas phase in the axial (y-axis) direction; Y was the axial (y-axis) distance.

For the first order ozone decomposition reaction, the reaction rate constant was independent of the gas concentration, and was given by Eq. 2. Substitution of Eq. 2 in Eq. 10 gave:

$$v_y \varepsilon_g \frac{dC_{O_3}}{dY} = -KC_{O_3}\varepsilon_s \tag{11}$$

where, K was the effective rate constant.

Chalermsinsuwan et al.[5] utilized the concept of equating the external mass transfer in terms of the global rate to the mass transfer from bulk gas to the catalyst surface at steady state,[4,31,32] to use the overall resistance from Eq. 11 to give the mass transfer coefficient as:

$$\frac{1}{K} = \frac{1}{k_{\text{mass transfer}} a_v} + \frac{1}{k_{\text{reaction}}} \tag{12}$$

where, $k_{\text{mass transfer}}$ was the mass transfer coefficient; a_v was the surface area per unit volume of a spherical particle.

The Sherwood number was given as:

$$Sh = \frac{k_{\text{mass transfer}} d_p}{D_{\text{diff.}}} \tag{13}$$

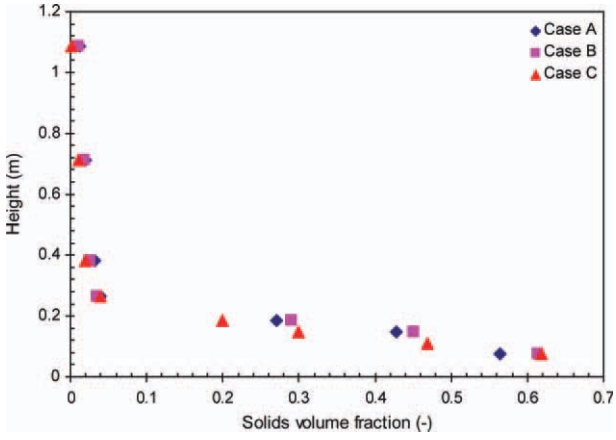

Figure 4. Axial variations of measured solids volume fractions, for Cases A, B, and C.

[Color figure can be viewed in the online issue, which is available at wileyonlinelibrary.com.]

where, *Sh* was the Sherwood number; D_{diff} was the molecular diffusivity equal to 2.88×10^{-5} m^2/s. Bolland and Nicolai[4] used a similar method to analyze the ozone decomposition data in their fluidized bed.

Measurements of reaction rate constants

The experiments were not designed to obtain precise reaction rate constants for the ozone decomposition reaction, but they were designed to obtain the mass transfer coefficients and Sherwood numbers. Hence, the precise measurements for the reaction rate constants were not needed, as long as they were in the range of the literature values. However, the procedure for the measurements of the reaction rate constants is described in this section.

The measurements of the reaction rate constants in this study were obtained in a fluidized bed instead of a fixed bed reactor,[9–11] using ozone concentrations and solids volume fractions. This was in view of the attempt to explain mass transfer phenomena in a bubbling fluidized bed.

For the measurements of effective rate constants in the differential reactor, C_{O_3} and ε_s in Eq. 11 were the average concentrations of ozone and catalyst, respectively, taken between pairs of consecutive points along the axial direction (*y*-axis), separated by a distance, *Y*. At low solids velocities, the product of the actual gas velocity and the voidage in Eq. 11 could be represented as the superficial gas velocity.[25] Values of the ozone concentrations and solids volume fractions were obtained from the data presented in Figures 3 and 4, respectively.

Hence, in the differential reactor, Eq. 11 was rewritten as:

$$U_g \frac{(C_{O_3(2)} - C_{O_3(1)})}{(Y_2 - Y_1)} = -K \frac{(C_{O_3(1)} + C_{O_3(2)})}{2} \frac{(\varepsilon_{s_1} + \varepsilon_{s_2})}{2} \quad (14)$$

where, U_g was the superficial gas velocity; Y_1, Y_2 were axial positions; $C_{O_3(1)}$, $C_{O_3(2)}$ were ozone concentrations at axial positions, Y_1 and Y_2, respectively; ε_{s_1}, ε_{s_2} were solids volume fractions at axial positions, Y_1 and Y_2, respectively.

Here, $C_{O_3} = \frac{(C_{O_3(1)} + C_{O_3(2)})}{2}$ and $\varepsilon_s = \frac{(\varepsilon_{s_1} + \varepsilon_{s_2})}{2}$ were the average concentrations of ozone and catalyst, respectively, between two axial points, separated by a distance of $Y = Y_2 - Y_1$.

Substitution of all the parameters in Eq. 14 gave the effective rate constant, K, between pairs of consecutive points along the axial (*y*-axis) direction, as shown in Figure 5. The effective rate constants at the lowest superficial gas velocity, 0.289 m/s, were high in the free board region due to the absence of significant amount of solids, as expected from Eq. 11.

Figure 5 shows that the effective rate constant is not only a local property, but is also a function of superficial gas velocity. The bubbling fluidized bed can be divided into the dense bubbling region at the bottom and the dilute cluster or free board region at the top. The effective rate constant in the bubbling region was much smaller than that in the cluster region. This was due to the fact that the bed was denser in the bubbling region than in the free-board or cluster region, leading to the formation of bigger and denser clusters in the bubbling region. The resistance to mass transfer was assumed to be small in the cluster region, thus, the system was not mass transfer controlled in that region. After neglecting the mass transfer resistance in Eq. 12, the reaction rate constant was equated to the effective rate constant in the free board region. The reaction rate constant was measured in the free board region, as both the resistances due to mass transfer and reaction were significant in the bubbling region, thus, making it incorrect to neglect the mass transfer resistance in that region. Hence, the mass transfer resistance was neglected in the region where the resistance due to reaction was more significant than the mass transfer resistance.

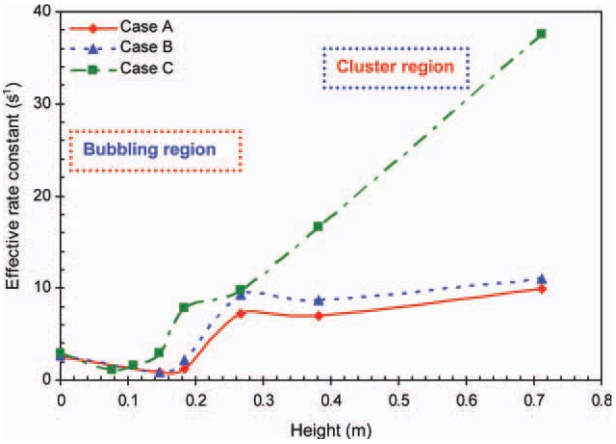

Figure 5. Axial variations of the effective rate constants, at three different superficial gas velocities.

[Color figure can be viewed in the online issue, which is available at wileyonlinelibrary.com.]

The effective rate constant was made independent of the superficial gas velocity in the free board region, in order to make the reaction rate constant independent of the superficial gas velocity in the same region.[29] The linear equations for the effective rate constant vs. superficial gas velocity were solved in pairs, in the free board region, at the heights of 0.71, 0.38, and 0.27 m, to obtain the effective rate constant independent of the superficial gas velocity. The results obtained at the lowest superficial gas velocity of 0.289 m/s were not included in the measurements of the reaction rate constants due to the presence of extremely low amount of particles in the free board region at that superficial gas velocity.

Table 2 shows that the values of the measured reaction rate constants in this study were 15.53, 8.47, and 5.62 s^{-1}. Table 3 shows that the values of the reaction rate constants for the ozone decomposition reaction on the surface of catalyst FCC particles were found to vary by at least three orders of magnitude in Refs. 4,9–11 and 22. The reaction rate constants measured using the 1-D conservation of species equation in this study, with values between 5.62 and 15.53 s^{-1}, were in reasonable agreement with those obtained by other authors from experiments. Hence, the use of these reaction rate constants in carrying out experiments and CFD simulations in 2- and 3-D systems described later was justified. However, the differences in the values of the reaction rate constants for the first order ozone decomposition reactions were due to different activities of the catalyst, and the temperature and humidity conditions during the experiments. For example, Breault[6] stated that the ozone decomposition reaction highly depends upon the moisture content.

Table 2. Measured Reaction Rate Constants by Solving in Pairs the Equations for the Effective Rate Constants as Functions of Two Superficial Gas Velocities

Heights Used to Solve Linear Equations (m)	0.711 and 0.381	0.711 and 0.267	0.381 and 0.267
$k_{reaction}$ (s^{-1})	15.53	8.47	5.62

Furthermore, van Swaaij and Zuiderweg[33] stated that the value of the reaction rate constant for the ozone decomposition reaction highly depends upon both temperature and humidity.

Measurements of Mass Transfer Coefficient and Sherwood Number

The mass transfer coefficients and Sherwood numbers in the bubbling fluidized bed were calculated using Eqs. 12 and 13, respectively. Table 4 summarizes the measured mass transfer coefficients and Sherwood numbers in the bubbling and cluster regions, at three different superficial gas velocities, at the heights of (A) 0, (B) 0.076, (C) 0.108, (D) 0.146, (E) 0.184, (F) 0.267, (G) 0.381, and (H) 0.711 m, with various reaction rate constants shown in Table 2. The mass transfer coefficients and Sherwood numbers were measured at various axial levels (y-axis), and radially and tangentially at the center ($r/R = 0$; $z/Z = 0$). The dependence of the mass transfer coefficient and Sherwood number on the reaction rate constant supports the results obtained in the literature (Solbrig and Gidaspow,[34] Kulacki and Gidaspow,[35] and Bird et al.[36]). The measured mass transfer coefficients and Sherwood numbers in the bubbling and cluster regions were of the orders of 10^{-5}–10^{-3} m/s and 10^{-5}–10^{-3} (-), respectively. These values lied reasonably well in the lower Reynolds number ($\mathrm{Re_p} = \frac{\rho_g d_p U_g}{\mu_g} = 1.47, 1.71, 1.74$) region in the literature comparison of the Sherwood numbers by Breault[6] and Breault and Guenther,[7] as described later in Figure 16. It was observed that similar to the dispersion coefficients (Refs. 37 and 38), the mass transfer coefficients and Sherwood numbers were also local quantities that changed with the position inside the fluidized bed.

Table 4 shows that for low reaction rate constants of 5.62 and 8.47 s^{-1}, the resistances due to reaction were too high at some locations, especially in the free board region, that the reaction controlled the system at those locations. However, for high reaction rate constant of 15.53 s^{-1}, the diffusion resistances became large and were computed using the concept of additive diffusional and chemical reaction resistances. In view of the fact that the overall effective rate constant was close to the reaction rate constant, the mass transfer was reasonably good. However, the reason for low Sherwood number was its direct dependence on the particle diameter. Equation 13 was rewritten as:

$$Sh = \frac{k_{\text{mass transfer}} d_p}{D_{\text{diff.}}} = \frac{6 k_{\text{mass transfer}}}{a_v D_{\text{diff.}}} \tag{15}$$

Equation 15 shows that for small particles or large surface area per unit volume of particles, the mass transfer coefficient had to be extremely high to give a Sherwood number of two. The formation of particle clusters in the bubbling fluidized bed decreased the mass transfer due to the restriction of movement of gas into the dense clusters. However, the mass transfer was not as poor as it was implied by the extremely small values of the Sherwood numbers, which depend upon the diameter of particles, not clusters.

Kashyap[29] shows the formation of bubbles and clusters in the riser section of the IIT 2-D CFB, under conditions similar to those utilized in this study. The largest cluster in the free board region was of the order of 0.14 m, whereas, the largest bubble in the bubbling region was of the order of 0.11 m. Table 4 shows that the substitution of cluster and bubble sizes in place of the particle diameter, in Eq. 13 for the Sherwood number for particles, gave the Sherwood numbers for clusters ($Sh_c = \frac{Sh_p d_c}{d_p}$) in the free board region and for bubbles ($Sh_b = \frac{Sh_p d_b}{d_p}$) in the bubbling region three orders of magnitude higher than those for the particles. This shows that the convection to diffusion ratio for fine particles was lower than that for large particles, which do not form clusters. In addition, for the diffusion limit of two for the Sherwood number, the estimated cluster and bubble diameters are shown in Table 4. The calculated cluster and bubble sizes varied between 0.05 and 5 m for the Sherwood number of two. An example of the measurement of mass transfer coefficient and Sherwood number is shown in Appendix.

CFD Simulations Using Kinetic Theory Based Model in FLUENT

This section of the paper describes the 3- and 2-D CFD simulations performed by considering the ozone decomposition reaction in the bubbling fluidized bed used in the experimental section of this study. The simulations were performed in the riser section of the IIT 2-D CFB, using a standard kinetic theory based model described in Gidaspow[25] and Gidaspow and Jiradilok,[39] and available in MFIX and the commercial code, FLUENT 6.2.16 (Fluent[40]), with the Energy Minimization Multi-Scale (EMMS) interphase exchange coefficient or drag model. The model was used to compare the computed mass transfer coefficients and Sherwood numbers with the measured values.

The bubbles in the bubbling bed usually do not contain almost any particles. Therefore, there should be almost negligible decomposition of ozone inside the bubbles, as the rate of ozone decomposition reaction is directly proportional to solids volume fraction (Eqs. 10 and 11). In order to avoid the computation of reaction inside the bubbles, the clusters and bubbles need to be resolved properly. Otherwise, the inability to resolve the clusters and bubbles could result in

Table 3. Ozone Decomposition Reaction Rate Constants from Experimental Studies in the Literature

Authors	Reaction Rate Constant (s^{-1})
Fryer and Potter (1976)	0.049–7.75
Jiang et al. (1991)	2.8–5.1
Ouyang et al. (1993)	3.96
Ouyang et al. (1995)	14.18–57.2
Bolland and Nicolai (2001)	26–62
This study	15.53, 8.47, 5.62

Table 4. Measured Mass Transfer Coefficients and Sherwood Numbers at Different Axial Positions in the IIT 2-D Fluidized Bed, for Cases A, B, and C, Using Additive Resistances (Bubble and Cluster Diameters were Calculated from Pictures Given in Kashyap[29])

$a_v = 78{,}947\ m^{-1}$

Case	U_g (m/s)	$k_{reaction}$ (s^{-1})	K at the Bottom of Bubbling Bed ($H_0 = 0$) (s^{-1})	$k_{mass\ tranfer}$ (m/s)	Sh_p (−)	d_b (m)	Sh_b (−)	$Sh_{diff.\ limit}$ (−)	$d_{c\ (diff.)}$ (m)	Re_p (−)
C	0.289	15.53	2.91	4.54E-05	0.00012	0.11	0.174	2	1.27	1.47
B	0.337	15.53	2.66	4.06E-05	0.00011	0.11	0.155	2	1.42	1.71
A	0.343	15.53	2.55	3.86E-05	0.00010	0.11	0.148	2	1.49	1.74
C	0.289	8.47	2.91	5.62E-05	0.00015	0.11	0.215	2	1.02	1.47
B	0.337	8.47	2.66	4.91E-05	0.00013	0.11	0.187	2	1.17	1.71
A	0.343	8.47	2.55	4.62E-05	0.00012	0.11	0.176	2	1.25	1.74
C	0.289	5.62	2.91	7.67E-05	0.00020	0.11	0.293	2	0.75	1.47
B	0.337	5.62	2.66	6.39E-05	0.00017	0.11	0.244	2	0.90	1.71
A	0.343	5.62	2.55	5.91E-05	0.00016	0.11	0.226	2	0.97	1.74

Case	U_g (m/s)	$k_{reaction}$ (s^{-1})	K at $H_1 = 0.076$ m (s^{-1})	$k_{mass\ transfer}$ (m/s)	Sh_p (−)	d_c (m)	Sh_c (−)	$Sh_{diff.\ limit}$ (−)	$d_{c\ (diff.)}$ (m)	Re_p (−)
C	0.289	15.53	1.09	1.48E-05	0.00004	0.14	0.072	2	3.89	1.47
B	0.337	15.53	–	–	–	–	–	–	–	–
A	0.343	15.53	–	–	–	–	–	–	–	–
C	0.289	8.47	1.09	1.58E-05	0.00004	0.14	0.077	2	3.65	1.47
B	0.337	8.47	–	–	–	–	–	–	–	–
A	0.343	8.47	–	–	–	–	–	–	–	–
C	0.289	5.62	1.09	1.71E-05	0.00005	0.14	0.083	2	3.37	1.47
B	0.337	5.62	–	–	–	–	–	–	–	–
A	0.343	5.62	–	–	–	–	–	–	–	–

Case	U_g (m/s)	$k_{reaction}$ (s^{-1})	K at $H_2 = 0.108$ m (s^{-1})	$k_{mass\ transfer}$ (m/s)	Sh_p (−)	d_c (m)	Sh_c (−)	$Sh_{diff.\ limit}$ (−)	$d_{c\ (diff.)}$ (m)	Re_p (−)
C	0.289	15.53	1.58	2.23E-05	0.00006	0.14	0.109	2	2.58	1.47
B	0.337	15.53	–	–	–	–	–	–	–	–
A	0.343	15.53	–	–	–	–	–	–	–	–
C	0.289	8.47	1.58	2.47E-05	0.00007	0.14	0.120	2	2.34	1.47
B	0.337	8.47	–	–	–	–	–	–	–	–
A	0.343	8.47	–	–	–	–	–	–	–	–
C	0.289	5.62	1.58	2.79E-05	0.00007	0.14	0.136	2	2.06	1.47
B	0.337	5.62	–	–	–	–	–	–	–	–
A	0.343	5.62	–	–	–	–	–	–	–	–

Case	U_g (m/s)	$k_{reaction}$ (s^{-1})	K at $H_3 = 0.146$ m (s^{-1})	$k_{mass\ transfer}$ (m/s)	Sh_p (−)	d_c (m)	Sh_c (−)	$Sh_{diff.\ limit}$ (−)	$d_{c\ (diff.)}$ (m)	Re_p (−)
C	0.289	15.53	2.89	4.49E-05	0.00012	0.14	0.218	2	1.28	1.47
B	0.337	15.53	0.84	1.13E-05	0.00003	0.14	0.055	2	5.10	1.71
A	0.343	15.53	0.91	1.23E-05	0.00003	0.14	0.06	2	4.68	1.74
C	0.289	8.47	2.89	5.55E-05	0.00015	0.14	0.27	2	1.04	1.47
B	0.337	8.47	0.84	1.19E-05	0.00003	0.14	0.058	2	4.85	1.71
A	0.343	8.47	0.91	1.30E-05	0.00003	0.14	0.063	2	4.43	1.74
C	0.289	5.62	2.89	7.53E-05	0.0002	0.14	0.366	2	0.76	1.47
B	0.337	5.62	0.84	1.26E-05	0.00003	0.14	0.061	2	4.58	1.71
A	0.343	5.62	0.91	1.38E-05	0.00004	0.14	0.067	2	4.16	1.74

Case	U_g (m/s)	$k_{reaction}$ (s^{-1})	K at $H_4 = 0.184$ m (s^{-1})	$k_{mass\ transfer}$ (m/s)	Sh_p (−)	d_c (m)	Sh_c (−)	$Sh_{diff.\ limit}$ (−)	$d_{c\ (diff.)}$ (m)	Re_p (−)
C	0.289	15.53	7.80	1.99E-04	0.00052	0.14	0.966	2	0.29	1.47
B	0.337	15.53	2.25	3.34E-05	0.00009	0.14	0.162	2	1.72	1.71
A	0.343	15.53	1.27	1.75E-05	0.00005	0.14	0.085	2	3.30	1.74
C	0.289	8.47	7.80	1.25E-03	0.00329	0.14	6.070	2	0.05	1.47
B	0.337	8.47	2.25	3.89E-05	0.00010	0.14	0.189	2	1.48	1.71
A	0.343	8.47	1.27	1.89E-05	0.00005	0.14	0.092	2	3.05	1.74
C	0.289	5.62	7.80	–	–	0.14	–	2	–	1.47
B	0.337	5.62	2.25	4.77E-05	0.00013	0.14	0.232	2	1.21	1.71
A	0.343	5.62	1.27	2.07E-05	0.00005	0.14	0.101	2	2.78	1.74

(*Continued*)

Table 4. (Continued)

$a_v = 78{,}947\ m^{-1}$										
Case	U_g (m/s)	$k_{reaction}$ (s^{-1})	K at $H_5 = 0.267$ m (s^{-1})	$k_{mass\ transfer}$ (m/s)	Sh_p (−)	d_c (m)	Sh_c (−)	$Sh_{diff.\ limit}$ (−)	$d_{c\ (diff.)}$ (m)	Re_p (−)
C	0.289	15.53	9.80	3.37E-04	0.00089	0.14	1.636	2	0.17	1.47
B	0.337	15.53	9.32	2.95E-04	0.00078	0.14	1.435	2	0.20	1.71
A	0.343	15.53	7.23	1.72E-04	0.00045	0.14	0.834	2	0.34	1.74
C	0.289	8.47	9.80	–	–	0.14	–	2	–	1.47
B	0.337	8.47	9.32	–	–	0.14	–	2	–	1.71
A	0.343	8.47	7.23	6.26E-04	0.00165	0.14	3.043	2	0.09	1.74
C	0.289	5.62	9.80	–	–	0.14	–	2	–	1.47
B	0.337	5.62	9.32	–	–	0.14	–	2	–	1.71
A	0.343	5.62	7.23	–	–	0.14	–	2	–	1.74
Case	U_g (m/s)	$k_{reaction}$ (s^{-1})	K at $H_6 = 0.381$ m (s^{-1})	$k_{mass\ transfer}$ (m/s)	Sh_p (−)	d_c (m)	Sh_c (−)	$Sh_{diff.\ limit}$ (−)	$d_{c\ (diff.)}$ (m)	Re_p (−)
C	0.289	15.53	16.66	–	–	0.14	–	2	–	1.47
B	0.337	15.53	8.66	2.48E-04	0.00065	0.14	1.205	2	0.23	1.71
A	0.343	15.53	6.95	1.59E-04	0.00042	0.14	0.774	2	0.36	1.74
C	0.289	8.47	16.66	–	–	0.14	–	2	–	1.47
B	0.337	8.47	8.66	–	–	0.14	–	2	–	1.71
A	0.343	8.47	6.95	4.88E-04	0.00129	0.14	2.373	2	0.12	1.74
C	0.289	5.62	16.66	–	–	0.14	–	2	–	1.47
B	0.337	5.62	8.66	–	–	0.14	–	2	–	1.71
A	0.343	5.62	6.95	–	–	0.14	–	2	–	1.74
Case	U_g (m/s)	$k_{reaction}$ (s^{-1})	K at $H_7 = 0.711$ m (s^{-1})	$k_{mass\ transfer}$ (m/s)	Sh_p (−)	d_c (m)	Sh_c (−)	$Sh_{diff.\ limit}$ (−)	$d_{c\ (diff.)}$ (m)	Re_p (−)
C	0.289	15.53	37.56	–	–	0.14	–	2	–	1.47
B	0.337	15.53	11.01	4.79E-04	0.00126	0.14	2.329	2	0.12	1.71
A	0.343	15.53	9.88	3.44E-04	0.00091	0.14	1.673	2	0.17	1.74
C	0.289	8.47	37.56	–	–	0.14	–	2	–	1.47
B	0.337	8.47	11.01	–	–	0.14	–	2	–	1.71
A	0.343	8.47	9.88	–	–	0.14	–	2	–	1.74
C	0.289	5.62	37.56	–	–	0.14	–	2	–	1.47
B	0.337	5.62	11.01	–	–	0.14	–	2	–	1.71
A	0.343	5.62	9.88	–	–	0.14	–	2	–	1.74

mismatching of the ozone concentrations along the axial direction in the fluidized bed. Besides, in real situations, in the core-annular regime, there is bypassing of gas in the center of the fluidized bed of FCC particles, along the tangential (z-axis) direction, which is difficult to compute using a 2-D geometry. Hence, this section of the paper presents results from extremely fine meshes/grids in 3- and 2-D computational domains. However, Xie et al.[41] studied the effect of dimensions in fluidized bed simulations, and found that the 2-D geometry using Cartesian and cylindrical coordinates could be successfully used to simulate the hydrodynamics in the bubbling bed regimes.

Hydrodynamic model

The hydrodynamic model used in FLUENT is described in Table 5. The model used the principle of solving Navier-Stokes equations. The basic equations numerically solved in the code were the conservation of mass, momentum, energy, and gas species, and constitutive equations, for gas and solid phases, using Eulerian-Eulerian approach,[25,39,42] where each phase was considered continuum. The model incorporated the kinetic theory of granular flow, as reported by Neri and Gidaspow.[43]

A more detailed description of the kinetic theory model used in FLUENT can be obtained from Fluent.[44] The EMMS drag model,[45,46] which is a modification of the Wen and Yu[47] drag law, and was developed using the concept of particle clusters, was used in this study.

System description and computational domain

The CFD simulations were performed for Cases 1 to 13, for the fluidized bed shown in Figure 1, by varying the (1) superficial gas velocity; (2) reaction rate constant; (3) mesh/grid sizes; (4) initial particle bed height; and (5) geometry between three- and two-dimensions. All the simulations were performed under bubbling fluidization conditions. The computational domains for the 3- and 2-D geometries, with defined x, y, and z directions, are shown in Figures 6A, B, respectively.

The 3- and 2-D geometries had tetrahedral/hybrid and quadrilateral type meshes, respectively. The total numbers of cells in the 3-D geometry were around 35,000 and 100,000, whereas, the total number of cells in the 2-D geometry were around 24,000. The riser section had inner width and height of 0.3048 and 1.283 m, respectively. The depth of the riser section in 3-D geometry was 0.051 m. The bottom inlets for the mixture of air and ozone were divided into twelve equal width rectangles and lines in 3- and 2-D geometries, respectively. This was done to be able to use nonuniform gas velocity profiles at the inlets. The outlet size on the right side of the bubbling fluidized bed was 0.152 m.

Table 5. Kinetic Theory Based Hydrodynamic Model for FLUENT

Conservation of mass or continuity equations

1. Gas phase:

$$\frac{\partial(\rho_g \varepsilon_g)}{\partial t} + \nabla \cdot (\rho_g \varepsilon_g v_g) = 0$$

2. Solid phase:

$$\frac{\partial(\rho_s \varepsilon_s)}{\partial t} + \nabla \cdot (\rho_s \varepsilon_s v_s) = 0$$

Conservation of momentum equations

1. Gas phase

$$\frac{\partial(\rho_g \varepsilon_g v_g)}{\partial t} + \nabla \cdot (\rho_g \varepsilon_g v_g v_g) = -\varepsilon_g \nabla P_g + \nabla \cdot \bar{\bar{\tau}}_g - \beta_A (v_g - v_s) + \varepsilon_g \rho_g g$$

2. Solid phase

$$\frac{\partial(\rho_s \varepsilon_s v_s)}{\partial t} + \nabla \cdot (\rho_s \varepsilon_s v_s v_s) = -\varepsilon_s \nabla P - \nabla P_s + \nabla \cdot \bar{\bar{\tau}}_s + \beta_A (v_g - v_s) + \varepsilon_s (\rho_s - \rho_g) g$$

Conservation of fluctuating energy equation for particles ($\theta = \frac{1}{3} . < C^2 >$)

$$\frac{3}{2}\left[\frac{\partial}{\partial t}(\varepsilon_s \rho_s \theta) + \nabla \cdot (\varepsilon_s \rho_s v_s \theta)\right] = \left(-\nabla P_s \bar{\bar{I}} + \bar{\bar{\tau}}_s\right) : \nabla v_s + \nabla \cdot (\kappa_s \nabla \theta) - \gamma_s + \phi_{ls}$$

Conservation of energy equations

1. Gas phase

$$\frac{\partial}{\partial t}(\varepsilon_g \rho_g h_g) + \nabla . (\varepsilon_g \rho_g v_g h_g) = -\varepsilon_g \frac{\partial P_g}{\partial t} + \bar{\bar{\tau}}_g : \nabla . v_g + S_g + Q_{sg}$$

with, $h_g = \int c_{pg}\, dT_g$

2. Solid phase

$$\frac{\partial}{\partial t}(\varepsilon_s \rho_s h_s) + \nabla . (\varepsilon_s \rho_s v_s h_s) = -\varepsilon_s \frac{\partial P_s}{\partial t} + \bar{\bar{\tau}}_s : \nabla . v_s + S_s + Q_{gs}$$

with, $h_s = \int c_{ps}\, dT_s$

Conservation of species equations (I = O_3, O_2 or N_2 (air))

$$\frac{\partial}{\partial t}(\varepsilon_g \rho_g y_i) + \nabla . (\varepsilon_g \rho_g v_g y_i) = r_i$$

Constitutive equations

1. Definitions

$$\varepsilon_g + \varepsilon_s = 1$$

2. Gas pressure

$$P_g = \rho_g RT_g$$

3. Stress tensor (ph. = gas or solid)

where,

$$\overline{\overline{D_{m,\,ph.}}} = \frac{1}{2}[\nabla v_{ph.} + (\nabla v_{ph.})^T]$$

4. Solid phase pressure

$$P_s = \rho_s \varepsilon_s \theta [1 + 2(1 + e) g_0 \varepsilon_s]$$

Table 5. (Continued)

5. Solid phase shear viscosity

$$\mu_s = \frac{10 \rho_s d_p \sqrt{\pi \theta}}{96(1+e) g_o \varepsilon_s}\left[1 + \frac{4}{5}(1+e) g_o \varepsilon_s\right]^2 + \frac{4}{5}\varepsilon_s \rho_s d_p g_o (1+e)\sqrt{\frac{\theta}{\pi}}$$

6. Solid phase bulk viscosity

$$\lambda_s = \frac{4}{3}\varepsilon_s \rho_s d_p g_o (1 + e)\sqrt{\frac{\theta}{\pi}}$$

where, g_0 is the radial distribution function

$$g_o = \left[1 - \left(\frac{\varepsilon_s}{\varepsilon_{s,max}}\right)^{1/3}\right]^{-1}$$

7. Collisional dissipation of solid fluctuation energy

$$\gamma_s = 3(1 - e^2)\varepsilon_s^2 \rho_s g_o \theta \left(\frac{4}{d_s}\sqrt{\frac{\theta}{\pi}} - \nabla \cdot v_s\right)$$

8. Granular conductivity of fluctuating energy

$$\kappa_s = \frac{150 \rho_s d_p \sqrt{\pi \theta}}{384(1+e) g_o}\left[1 + \frac{6}{5}(1+e) g_o \varepsilon_s\right]^2 + 2\varepsilon_s^2 \rho_s d_p g_o (1+e)\sqrt{\frac{\theta}{\pi}}$$

9. Gas–solid drag coefficient (EMMS drag) for $\varepsilon_g < 0.74$ (based on the Ergun equation)

$$\beta_A = 150\frac{\varepsilon_s^2 \mu_g}{\varepsilon_g d_p^2} + 1.75\frac{\rho_g \varepsilon_s}{d_p}|v_g - v_s|$$

for $\varepsilon_g \geq 0.74$

$$\beta_A = \frac{3}{4} C_d \frac{\rho_g \varepsilon_s \varepsilon_g |v_g - v_s|}{d_p}\omega(\varepsilon_g)$$

when, $0.74 \leq \varepsilon_g \leq 0.82$, $\omega(\varepsilon_g) = -0.5760 + \frac{0.0214}{4(\varepsilon_g - 0.7463)^2 + 0.0044}$

when, $0.82 \leq \varepsilon_g \leq 0.97$, $\omega(\varepsilon_g) = -0.0101 + \frac{0.0038}{4(\varepsilon_g - 0.7789)^2 + 0.0040}$

when, $\varepsilon_g > 0.97$, $\omega(\varepsilon_g) = -31.8295 + 32.8295\varepsilon_g$

where,

$$C_d = \frac{24}{Re_p}\left[1 + 0.15\, Re_p^{0.697}\right] \quad \text{for} \quad Re_p < 1000$$

$$C_d = 0.44 \quad \text{for} \quad Re_p \geq 1000$$

$$Re_p = \frac{\varepsilon_g \rho_g d_p |v_g - v_s|}{\mu_g}$$

The restitution coefficients were 0.95 and 0.9 for the particle–particle and particle-wall collisions, respectively. The specularity coefficient was 0.0001. A reasonable time step of 1×10^{-3} s was used. The simulations in Cases 1 to 13 were run for 40 s. By reasonably assuming quasi-steady state, the simulation results were averaged for 15 s in each case, beyond 25 s. Table 6 presents the system geometry and properties for the CFD simulations using FLUENT, in Cases 1 to 13. The CFD simulations were performed on a 64-bit Dell Precision 690 workstation, with Intel® Xeon® 2.66 GHz CPU 2 GB RAM.

Initial and boundary conditions

The use of practical initial and boundary conditions was extremely essential in obtaining realistic results from the CFD simulations. In view of the fact that the superficial gas velocities in Cases A and B, in experiments, were very close

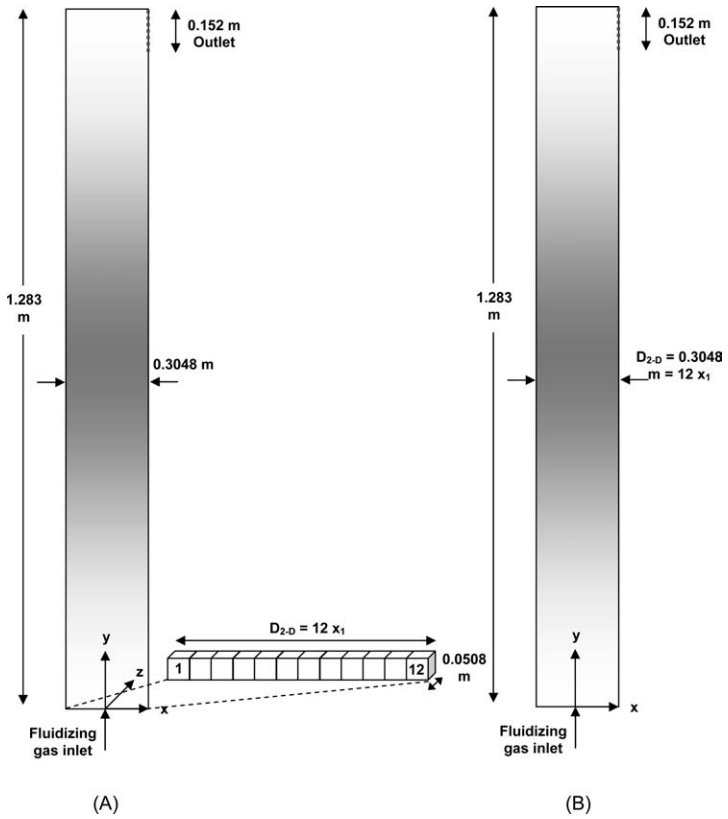

Figure 6. (A) 3- and (B) 2-D computational simulation domains for the riser section of the IIT 2-D CFB, using FLUENT.

to each other, the inlet superficial gas velocities employed in different cases in the CFD simulations were 0.343 and 0.289 m/s only. The simulation results were compared with the experiments at the superficial gas velocities of 0.343 and 0.289 m/s in Cases A and C, respectively. The reaction rate constants used in the simulations were 15.53, 8.47, and 5.62 s^{-1}, as obtained experimentally. The inlet ozone concentrations were 13.2 and 10.5 ppm at the superficial gas velocities of 0.343 and 0.289 m/s, respectively. There were no solids entering the fluidized bed from the bottom, as the fluidized bed was operated in the bubbling fluidization regime.

Initially, the fluidized bed was filled with particles up to a height of 0.0762 m in Cases 1 to 8 and Cases 10 to 13, as against 0.054 m in the experiments. This was due to the fact that during the experiments, there may have been a slight inflow of particles from the downcomer to the riser section through possible gaps between the temporary removable wall and the walls of the riser section, resulting in slight increase in the height of the bed. Besides, the CFD simulation results reasonably matched the measured ozone concentrations, mass transfer coefficients and the Sherwood numbers, by making such a minor change in the initial height. However, the initial height in Case 9 was 0.054 m.

A pressure of one atmosphere was specified at the outlet. A no-slip boundary condition was utilized for the gas phase velocities in the radial and axial directions at the walls. While the no-slip boundary condition was used for the radial solids velocity at the walls, the Johnson and Jackson[48] slip boundary condition was employed for the axial solids velocity at the walls. The Johnson and Jackson[48] granular temperature boundary condition was utilized for the granular temperature at the walls. Table 7 summarizes the initial and boundary conditions for the CFD simulations performed using the kinetic theory based model in FLUENT, considering the ozone decomposition reaction, for Cases 1 to 13.

Simulation Results

The main criteria for obtaining reliable results from the simulations were to reasonably match the ozone decomposition with the experimental data, and to support the measurements of low mass transfer coefficients and Sherwood numbers in this study.

The descriptions of the cases studied in this section of the paper were as follows: Cases 1 to 8 and Cases 10 to 13 had initial particle bed heights of 0.0762 m, whereas, Case 9 had an initial particle bed height of 0.054 m. Cases 1 to 9 utilized 3-D geometry. Cases 1, 2, and 3 had around 35,000 cells, with the reaction rate constants of 15.53, 8.47, and 5.62 s^{-1}, respectively. The inlet ozone concentration and superficial gas velocity in Cases 1, 2, and 3 were 13.2 ppm and 0.343 m/s, respectively. Case 4 was similar to Case 1, but with around 100,000 cells. In terms of the geometry, Cases 5, 6, and 7 were similar to Cases 1, 2, and 3, respectively. However, the inlet ozone concentration and superficial gas velocity in Cases 5, 6, and 7 were 10.5 ppm and 0.289 m/s, respectively. Case 8 was similar to Case 5, but had around 100,000 cells. Case 9 was similar to Case 1, but

Table 6. System Geometry and Properties for CFD Simulations Using FLUENT, in Cases 1 to 13

Geometry/Property	Case 1	Case 2	Case 3	Case 4	Case 5	Case 6	Case 7	Case 8	Case 9	Case 10	Case 11	Case 12	Case 13	Unit
Geometry type	3-D									2-D				–
Riser section width, $D_{2\text{-D}}$	0.3048													m
Riser section height, H	1.283													m
Riser section depth, $W_{2\text{-D}}$	0.051									–	–	–	–	m
Riser section's each bottom inlet width, $x_1 = \ldots = x_{12}$	0.0254													m
Riser section outlet size, D_{outlet}	0.152													m
Particle diameter, d_p	76													μm
Particle density, ρ_s	1654													kg/m^3
Packing fraction, $\varepsilon_{s,\,max}$	0.66													–
Acceleration due to gravity, g	9.81													m/s^2
Fluidizing gas	Air													
Operating temperature, T_g	298													K
Gas density, ρ_g	1.2													kg/m^3
Gas viscosity μ_g	1.8×10^{-5}													kg/(m-s)
Terminal velocity, U_t	0.28													m/s
Minimum fluidization velocity, U_{mf}	0.003													m/s
Particle–particle restitution coefficient, e	0.95													–
Particle-wall restitution coefficient, e_w	0.9													–
Specularity coefficient, ϕ	0.0001													–
Mesh properties														
Elements	Tetrahedral/hybrid			Tetrahedral/hybrid			Tetrahedral/hybrid		Tetrahedral/hybrid		Quadrilateral			
Type	TGrid			TGrid			TGrid		TGrid		Map			–
Interval size or count	0.011 size up to 0.254 m and 0.022 size above			0.007 size up to 0.254 m and 0.022 size above			0.011 size up to 0.254 m and 0.022 size above		0.007 size up to 0.254 m and 0.022 size above	0.011 size up to 0.254 m and 0.022 size above		100 count up to 0.254 m and 50 count above		–
Number of cells	34,680			103,912			34,680		103,912	34,680		24,000		–
Number of wall faces	7612			14,316			7612		14,316	7612		505		–
Number of interior faces	65339			200,244			65339		200,244	65339		46780		–
Time step (Δt)	1×10^{-3}													s
Steady state for time averaging, t_{steady}	25 to 40													s

Table 7. Initial, Boundary and Operating Conditions in FLUENT, for Cases 1 to 13

Condition	Case 1	Case 2	Case 3	Case 4	Case 5	Case 6	Case 7	Case 8	Case 9	Case 10	Case 11	Case 12	Case 13	Unit
Reaction rate constant, $k_{reaction}$	15.53	8.47	5.62	15.53	15.53	8.47	5.62	15.53	15.53	15.53	8.47	5.62	15.53	s^{-1}
Bottom inlet conditions														
Inlet ozone concentration, $C_{O_3(inlet)}$	13.2	13.2	13.2	13.2	10.5	10.5	10.5	10.5	13.2	13.2	13.2	13.2	10.5	PPM
Gas velocities, U_{g_1}, U_{g_2}, U_{g_3}, U_{g_4}, U_{g_5}, U_{g_6}, U_{g_7}, U_{g_8}, U_{g_9}, $U_{g_{10}}$, $U_{g_{11}}$, $U_{g_{12}}$, U_g	0, 0, 1.03, 0, 0, 1.03, 1.03, 0, 0, 1.03, 0, 0, $\overline{0.343}$				0, 0, 0.867, 0, 0, 0.867, 0.867, 0, 0, 0.867, 0, 0, $\overline{0.289}$				0, 0, 1.03, 0, 0, 1.03, 1.03, 0, 0, 1.03, 0, 0, $\overline{0.343}$				0, 0, 0.867, 0, 0, 0.867, 0.867, 0, 0, 0.867, 0, 0, $\overline{0.289}$	m/s
Solids volume fraction, ε_s								0						–
Initial/Patch conditions														
Bed height, H_{bed}					0.0762				0.054				0.0762	m
Gas velocity, $U_{g\ initial}$								0.7						m/s
Solids velocity, $U_{s\ initial}$								0.5						m/s
Solids volume fraction, $\varepsilon_{s\ initial}$								0.5						–
Granular temperature, $\theta_{initial}$								0.1						m^2/s^2
Outlet condition														
Pressure, P_{outlet}								1.01325×10^5						N/m^2
Boundary conditions														
Solid phase (Johnson and Jackson, 1987)														
Velocity: $v_{s,w} = -\frac{6\mu_s \varepsilon_{s,max}}{\sqrt{3}\pi\phi\rho_s\varepsilon_s g_0\sqrt{\theta}}\frac{\partial v_{s,w}}{\partial \hat{n}}$														m/s
Granular temperature: $\theta_w = -\frac{\kappa_s\theta}{\gamma_{s,w}}\frac{\partial\theta_w}{\partial\hat{n}} + \frac{\sqrt{3}\pi\phi\rho_s\varepsilon_s v_{s,slip}^2 g_0\theta^{3/2}}{6\varepsilon_{s,max}\gamma_{s,w}}$, where $\gamma_{s,w} = \frac{\sqrt{3}\pi\left(1-e_w^2\right)\varepsilon_s\rho_s g_0\theta^{3/2}}{4\varepsilon_{s,max}}$													m^2/s^2
Gas phase														
$v_{x,w} = v_{y,w} = 0$														m/s

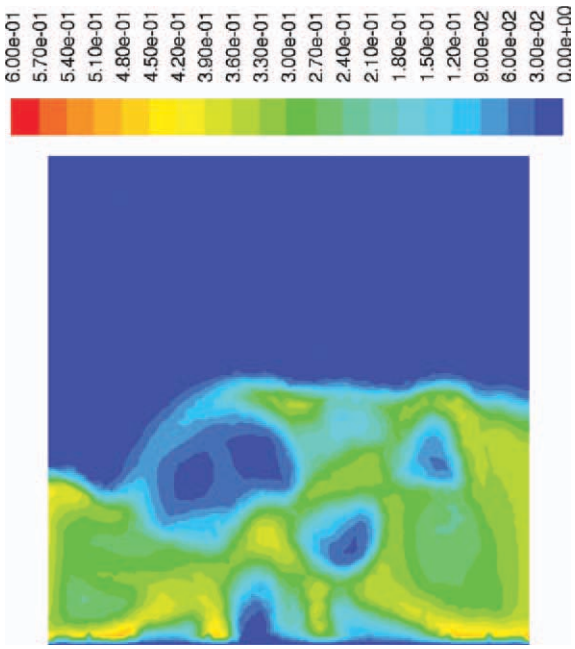

Figure 7. Close-up views of solids volume fractions in the riser section, at $z = 0$, in Case 8, at 40 s.

[Color figure can be viewed in the online issue, which is available at wileyonlinelibrary.com.]

with a different initial particle bed height. Cases 10 to 13 used 2-D geometries. Cases 10, 11, and 12 were similar to Cases 1, 2, and 3, respectively. Case 13 was similar to Case 5. This paper describes some of the important results, whereas, detailed results are given in Kashyap.[29]

Solids volume fraction distribution

Figure 7 shows a close-up view of the solids volume fraction in the bottom section of the bubbling fluidized bed, for Case 8. There was a clear coexistence of clusters and bubbles in the bubbling bed of Geldart A type particles, with solids concentrations of the bubbles and clusters being around 1 and 35% solids, respectively.

Figures 8A, B compare the time averaged axial profiles of the measured and computed solids volume fractions, between two mesh/grid sizes of 35,000 and 100,000 cells. Figures 8A, B were obtained at the superficial gas velocities of 0.343 and 0.289 m/s, respectively. The computed results among two different mesh/grid sizes at each superficial gas velocity were reasonably close to each other, showing that 35,000 cells were sufficient to obtain reasonable results. The computed solids volume fractions were significantly lower than the measured values at each superficial gas velocity, especially in the bubbling region. This could be due to the fact that there was a slight sticking of particles towards the walls of the fluidized bed in the experiments, leading to the measurements of high solids volume fractions. Besides, the solids volume fractions were measured tangentially averaged ($-1 \leq z/Z \leq 1$), as compared to the computations at tangentially centered ($z = 0$) locations. Although the tangential of the solids volume fractions were mostly flat, the profiles with extremely fine meshes/grids showed slight core-annular regimes at both superficial gas velocities.[29] This means that the measured tangentially averaged values of the solids volume fractions were somewhat higher than those computed tangentially at the center.

The comparisons of the time averaged axial profiles of the measured and computed solids volume fractions, between superficial gas velocities of 0.343 and 0.289 m/s, are shown in Kashyap.[29] The bed expansions in the experiments were higher than those in the computations. This could be related to the selection of the drag model from those currently available in the literature. The EMMS drag law has generally been used to simulate CFBs with relatively lower solids volume fractions, as against the bubbling fluidized beds. In addition, many researchers have successfully simulated bubbling fluidized beds of Geldart B type particles,[42,49] but there have not been significant reporting of computations in bubbling fluidized beds of Geldart A type particles. van Wachem et al.[50] showed that the hydrodynamics has high sensitivity to the drag model. McKeen and Pugsley[51] reported that the generally poor comparisons of the computed results for Geldart A particles with the experiments can be attributed to the existence of significant interparticle forces that are neglected in most simulations. They introduced a new scale factor, C_{drag}, to the drag model to take into account the other forces in the system. However, such changes in the drag laws are yet to be

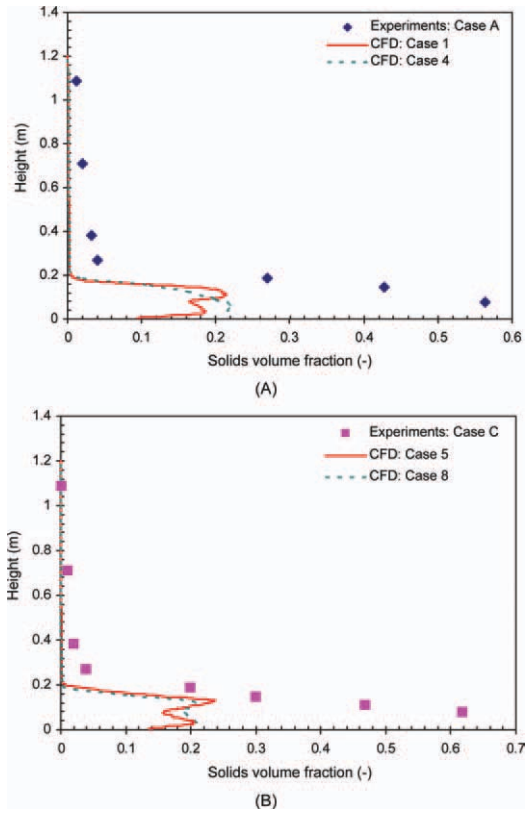

Figure 8. Comparison of measured and computed axial profiles of solids volume fractions, for different grid sizes, for (A) Cases A, 1 and 4, and (B) Cases C, 5 and 8.

[Color figure can be viewed in the online issue, which is available at wileyonlinelibrary.com.]

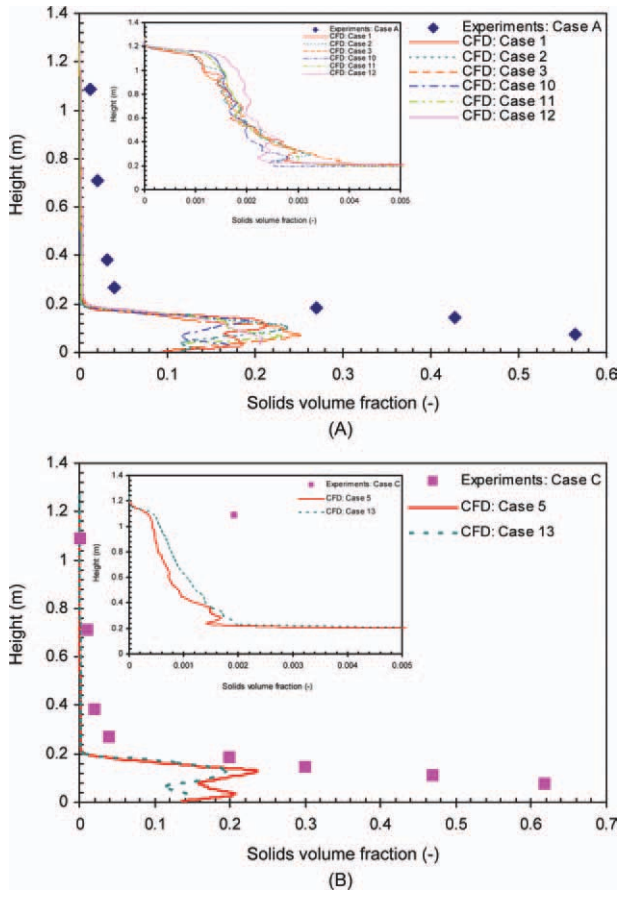

Figure 9. Comparison of measured and computed axial profiles of solids volume fractions, for 3- and 2-D geometries, for (A) Cases A, 1, 2, 3, 10, 11, and 12, and (B) Cases C, 5 and 13.

[Color figure can be viewed in the online issue, which is available at wileyonlinelibrary.com.]

proved successful to work universally in all the systems using Geldart A type particles.

In view of the fact that the experiments were designed to measure mass transfer coefficients, and not to get precise values of the reaction rate constants, the differences in the measured and computed solids volume fractions are reasonably acceptable.

Figures 9A, B compare the time averaged axial profiles of the measured and computed solids volume fractions, between 3- and 2-D geometries. Figures 9A, B were obtained at the superficial gas velocities of 0.343 and 0.289 m/s, respectively. The 2-D CFD simulations computed slightly higher solids volume fractions in the free board region than the 3-D CFD simulations. However, the 3-D CFD simulations computed slightly higher solids volume fractions than the 2-D CFD simulations, in the bubbling region. This could be due to slight differences in the actual gas velocities between the 3- and 2-D simulations, caused by the inability to accurately scale the 2-D system for the missing third dimension. This could also be due to accurate computation of dense clusters of particles by 3-D CFD simulations, leading to slightly higher solids volume fractions than those in the 2-D simulations. Overall, the differences in the values of the solids volume fractions computed by 3- and 2-D CFD simulations were not significant. Hence, in view of the fact that the 3-D CFD simulations were time-expensive, the conclusions by Xie et al.[41] that the 2-D CFD simulations can be used successfully to simulate the bubbling fluidized beds, were reasonable.

Ozone concentration distribution

The contour of the ozone concentration for Case 8, at 40 s, is shown in Figure 10. The inlet ozone concentration at the superficial gas velocity of 0.289 m/s was 10.5 ppm. The ozone concentration decreased upon moving up in the bubbling bed. However, the ozone was not completely decomposed inside the shallow bed of catalyzed particles. Ozone concentration contours for other cases studied in this research are given in Kashyap.[29]

Figure 11 shows the axial profiles of ozone concentrations for (A) experiments and 3-D CFD simulations at a superficial gas velocity of 0.343 m/s, and (B) experiments and 3-D CFD simulations at a superficial gas velocity of 0.289 m/s, with reaction rate constants of 15.53, 8.47, and 5.62 s^{-1}. As expected, the ozone decomposition reaction rate increased or the ozone concentration decreased, with the increase in the reaction rate constant. As stated earlier, the agreement between the computed and the measured ozone concentrations in the bubbling region was good at the reaction rate constant of 8.47 s^{-1}. However, the computed and measured ozone concentrations in the free board region agreed reasonably well with each other at the reaction rate constant of 15.53 s^{-1}. The deviations of the computed ozone concentrations from the measured values were due to high dependence of the reaction rate constant on the activity of the catalysts, and temperature and humidity conditions.

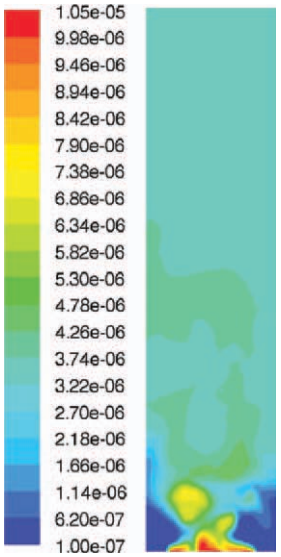

Figure 10. Ozone concentration contours in the riser section, at $z = 0$, in Case 8, at 40 s.

[Color figure can be viewed in the online issue, which is available at wileyonlinelibrary.com.]

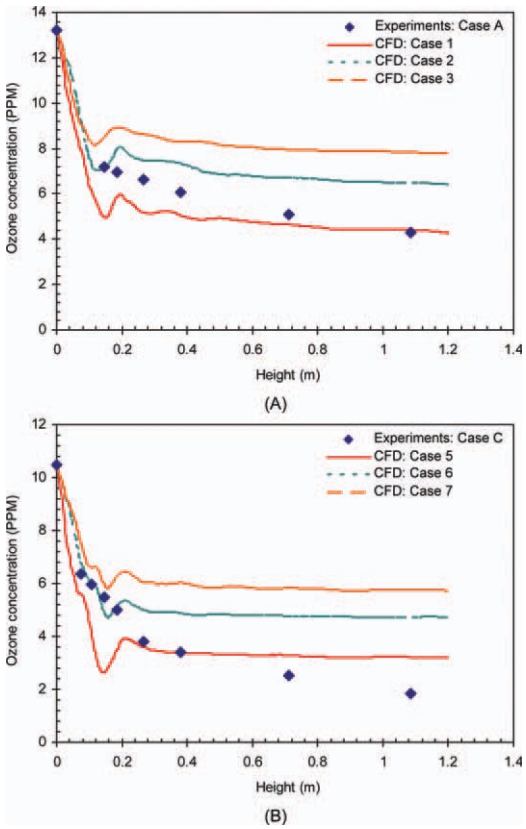

Figure 11. Comparison of measured and computed axial variations of ozone concentrations, for various reaction rate constants, for (A) Cases A, 1, 2 and 3, and (B) Cases C, 5, 6, and 7.

[Color figure can be viewed in the online issue, which is available at wileyonlinelibrary.com.]

Figures 12A, B compare the time averaged axial profiles of the measured and computed ozone concentrations, between two mesh/grid sizes of 35,000 and 100,000 cells. Figures 12A, B were obtained at the superficial gas velocities of 0.343 and 0.289 m/s, respectively. The finer mesh/grid model gave slightly better agreement with the measured values due to better resolution of bubbles and clusters. However, the differences were nearly inconspicuous. This shows that 35,000 cells were sufficient to obtain reasonable results, as the 100,000 cells utilized significant computational power.

Figure 13 shows a comparison of the time averaged axial profiles of the measured and computed ozone concentrations, considering initial particle bed heights of 0.0762 and 0.054 m, at a superficial gas velocity of 0.343 m/s and a reaction rate constant of 15.53 s^{-1}. The deviation of the computed ozone concentrations from the measured values in the bubbling region was higher with initial particle bed height of 0.054 m, as compared to that for 0.0762 m.

Figures 14A, B compare the time averaged axial profiles of the measured and computed ozone concentrations, between 3- and 2-D geometries. Figures 14A, B were obtained at the superficial gas velocities of 0.343 and 0.289 m/s, respectively. In the bubbling region, the 2-D CFD simulations computed ozone concentrations higher than those computed by the 3-D CFD simulations. However, in the free board region, the 3-D CFD simulations computed higher ozone concentrations than those computed by the 2-D CFD simulations. These trends could be supported by the opposite trends of the solids volume fractions shown in Figure 9.

The time averaged radial distributions of ozone concentrations at various heights, in Case 1, are shown in Figure 15. The profiles for other cases are given in Kashyap.[29] The profiles were almost opposite to the core-annular profile for solids volume fractions. The ozone concentration profiles were primarily flat in the free board region due to the absence of solids. In the dense region, up to a height of 0.184 m, the ozone concentrations were higher at the center than near the walls.[4,10,11] This was due to the high concentrations of solids near the walls.[10,11,52,53] The high solids volume fractions near the wall due to core-annular regime cause higher ozone decomposition rate as compared to that in the dilute core region.

Computation of Mass Transfer Coefficient and Sherwood Number

The methods used for the computation of mass transfer coefficients and Sherwood numbers were similar to those described in the experimental section of this paper. The

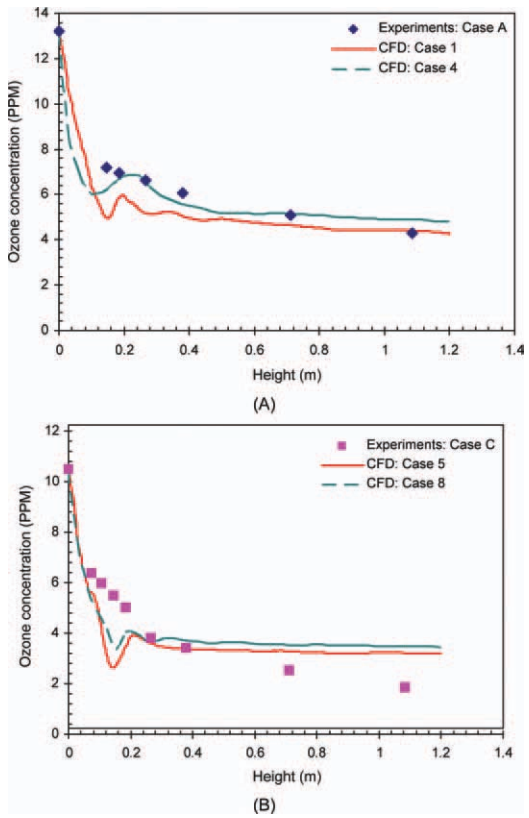

Figure 12. Comparison of measured and computed axial variations of ozone concentrations, for different grid sizes, for (A) Cases A, 1 and 4, and (B) Cases C, 5 and 8.

[Color figure can be viewed in the online issue, which is available at wileyonlinelibrary.com.]

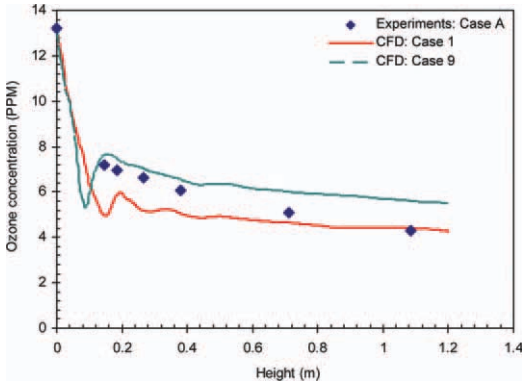

Figure 13. Comparison of measured and computed axial variations of ozone concentrations, at different initial bed heights, for Cases A, 1 and 9.

[Color figure can be viewed in the online issue, which is available at wileyonlinelibrary.com.]

mass transfer coefficients and Sherwood numbers in the bubbling fluidized bed were computed using Eqs. 12 and 13, respectively. Similar to the experiments, the effective rate constants in the differential reactor type bubbling fluidized bed for Cases 1 to 13 were computed using Eq. 14, where, C_{O_3} and ε_s were the average concentrations of ozone and FCC particles, respectively, taken between pairs of consecutive points along the axial direction (y-axis), separated by distance, Y. Hence, the effective rate constants were obtained between pairs of consecutive points along the axial (y-axis) direction. The computed effective rate constants were obtained from the solids volume fractions and ozone concentrations computed radially (x-axis) and tangentially (z-axis) at the center ($r/R = 0$; $z/Z = 0$).

The mass transfer coefficients and Sherwood numbers were computed at various axial levels (y-axis), and radially and tangentially at the center ($r/R = 0$; $z/Z = 0$), using Eqs. 12 and 13, respectively.

Table 8 summarizes the computed mass transfer coefficients and Sherwood numbers in the bubbling and cluster regions, for Cases 1 to 13, at the heights of (A) 0.076, (B) 0.108, (C) 0.146, (D) 0.184, (E) 0.267, and (F) 0.381 m. The computed mass transfer coefficients and Sherwood numbers were of the orders of 10^{-6}–10^{-3} m/s and 10^{-6}–10^{-2} (-), respectively. Figure 16A shows a reasonably good agreement between the measured and computed Sherwood numbers at low Reynolds numbers. Figure 16B shows a reasonably good agreement with the literature values summarized by Breault (2006) and Breault and Guenther (2009), particularly with those obtained by extrapolating the data by Bolland and Nicolai.[4] Figure 16 and Table 8 show that the mass transfer coefficients and Sherwood numbers were local quantities that changed with the location within the fluidized bed. This supports the reasoning by Breault[6] that the mass transfer coefficients and Sherwood numbers vary significantly due to different flow regimes and locations of data acquisition in the fluidized beds.

In the bubbling region, both the resistances due to reaction and mass transfer were comparable, and were computed

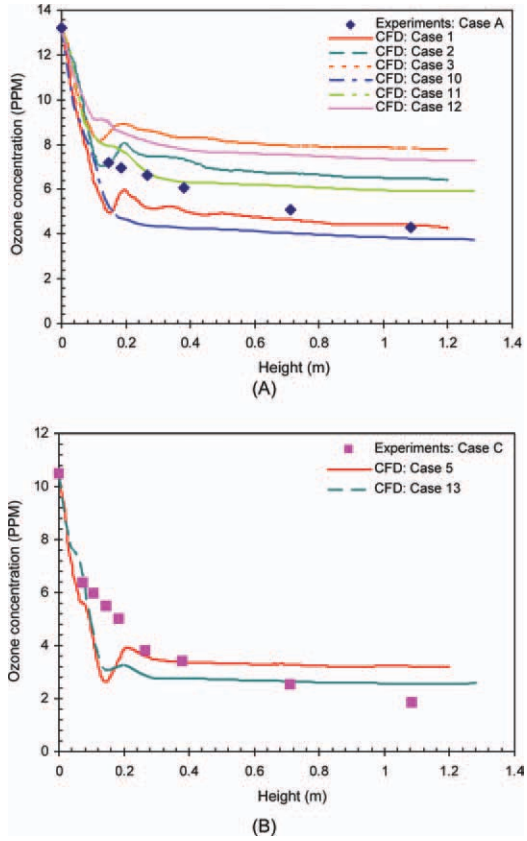

Figure 14. Comparison of measured and computed axial variations of ozone concentrations, for 3- and 2-D geometries, for (A) Cases A, 1, 2, 3, 10, 11 and 12, and (B) Cases C, 5 and 13.

[Color figure can be viewed in the online issue, which is available at wileyonlinelibrary.com.]

using the principle of additive resistances, using Eq. 12. However, in the free board region, the resistance due to reaction was much higher than the resistance due to mass transfer, causing inability to compute the later in that region.

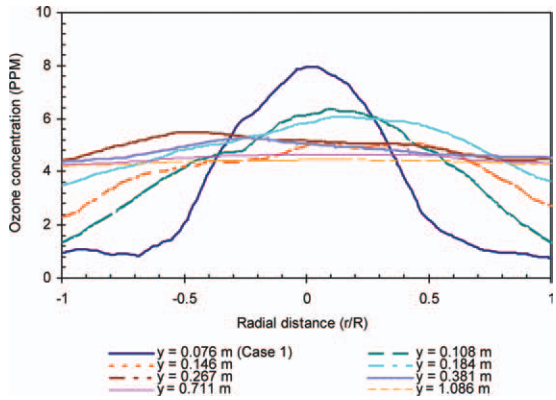

Figure 15. Radial distributions of ozone concentrations at various heights, for Case 1, at $z = 0$.

[Color figure can be viewed in the online issue, which is available at wileyonlinelibrary.com.]

Table 8. Computed Mass Transfer Coefficients and Sherwood Numbers at Different Axial Positions in the IIT 2-D Fluidized Bed, for Cases 1 to 13, Using additive Resistances (Bubble and Cluster Diameters were Obtained Roughly from the Solids Volume Fraction Contors)

$a_v = 78.947\ m^{-1}$										
Case	U_g (m/s)	$k_{reaction}$ (s^{-1})	K at $H_1 = 0.076$ m (s^{-1})	$k_{mass\ transfer}$ (m/s)	Sh_p (−)	d_b (m)	Sh_b (−)	$Sh_{diff.\ limit}$ (−)	$d_{b\ (diff.)}$ (m)	Re_p (−)
1	0.343	15.53	5.51	1.08E-04	0.00029	0.07	0.249	2	0.53	1.74
2	0.343	8.47	7.14	5.77E-04	0.00152	0.07	1.333	2	0.10	1.74
3	0.343	5.62	3.72	1.40E-04	0.00037	0.07	0.322	2	0.41	1.74
4	0.343	15.53	6.88	1.57E-04	0.00041	0.07	0.362	2	0.37	1.74
5	0.289	15.53	5.20	9.91E-05	0.00026	0.07	0.229	2	0.58	1.47
6	0.289	8.47	5.84	2.39E-04	0.00063	0.07	0.551	2	0.24	1.47
7	0.289	5.62	3.83	1.52E-04	0.00040	0.07	0.350	2	0.38	1.47
8	0.289	15.53	8.13	2.16E-04	0.00057	0.07	0.499	2	0.27	1.47
9	0.343	15.53	15.09	6.80E-03	0.01794	0.07	15.700	2	0.01	1.74
10	0.343	15.53	11.30	5.26E-04	0.00139	0.07	1.215	2	0.11	1.74
11	0.343	8.47	5.20	1.71E-04	0.00045	0.07	0.394	2	0.34	1.74
12	0.343	5.62	5.41	1.84E-03	0.00487	0.07	4.259	2	0.03	1.74
13	0.289	15.53	22.08	–	–	0.07	–	2	–	1.47
Case	U_g (m/s)	$k_{reaction}$ (s^{-1})	K at $H_2 = 0.108$ m (s^{-1})	$k_{mass\ transfer}$ (m/s)	Sh_p (−)	d_c (m)	Sh_c (−)	$Sh_{diff.\ limit}$ (−)	$d_{c\ (diff.)}$ (m)	Re_p (−)
1	0.343	15.53	10.78	4.46E-04	0.00118	0.07	1.029	2	0.13	1.74
2	0.343	8.47	7.94	1.59E-03	0.00421	0.07	3.681	2	0.04	1.74
3	0.343	5.62	2.18	4.50E-05	0.00012	0.07	0.104	2	1.28	1.74
4	0.343	15.53	0.36	4.73E-06	0.00001	0.07	0.011	2	12.18	1.74
5	0.289	15.53	24.54	–	–	0.07	–	2	–	1.47
6	0.289	8.47	1.91	3.12E-05	0.00008	0.07	0.072	2	1.85	1.47
7	0.289	5.62	0.13	1.64E-06	4.33E-06	0.07	0.004	2	35.13	1.47
8	0.289	15.53	7.48	1.83E-04	0.00048	0.07	0.422	2	0.32	1.47
9	0.343	15.53	–	–	–	0.07	–	2	–	1.74
10	0.343	15.53	17.07	–	–	0.07	–	2	–	1.74
11	0.343	8.47	3.07	6.10E-05	0.00016	0.07	0.141	2	0.94	1.74
12	0.343	5.62	0.73	1.06E-05	0.00003	0.07	0.024	2	5.44	1.74
13	0.289	15.53	21.55	–	–	0.07	–	2	–	1.47
Case	U_g (m/s)	$k_{reaction}$ (s^{-1})	K at $H_3 = 0.146$ m (s^{-1})	$k_{mass\ transfer}$ (m/s)	Sh_p (−)	d_c (m)	Sh_c (−)	$Sh_{diff.\ limit}$ (−)	$d_{c\ (diff.)}$ (m)	Re_p (−)
1	0.343	15.53	6.19	1.30E-04	0.00034	0.07	0.301	2	0.44	1.74
2	0.343	8.47	0.27	3.51E-06	0.00001	0.07	0.008	2	16.39	1.74
3	0.343	5.62	–	–	–	0.07	–	2	–	1.74
4	0.343	15.53	–	–	–	0.07	–	2	–	1.74
5	0.289	15.53	4.09	7.04E-05	0.00019	0.07	0.162	2	0.82	1.47
6	0.289	8.47	4.57	1.26E-04	0.00033	0.07	0.291	2	0.46	1.47
7	0.289	5.62	5.57	8.32E-03	0.02196	0.07	19.217	2	0.01	1.47
8	0.289	15.53	13.15	1.09E-03	0.00287	0.07	2.511	2	0.05	1.47
9	0.343	15.53	–	–	–	0.07	–	2	–	1.74
10	0.343	15.53	11.79	6.19E-04	0.00163	0.07	1.430	2	0.09	1.74
11	0.343	8.47	0.77	1.08E-05	0.00003	0.07	0.025	2	5.36	1.74
12	0.343	5.62	4.16	2.03E-04	0.00053	0.07	0.468	2	0.28	1.74
13	0.289	15.53	0.51	6.72E-06	0.00002	0.07	0.016	2	8.57	1.47
Case	U_g (m/s)	$k_{reaction}$ (s^{-1})	K at $H_4 = 0.184$ m (s^{-1})	$k_{mass\ transfer}$ (m/s)	Sh_p (−)	d_c (m)	Sh_c (−)	$Sh_{diff.\ limit}$ (−)	$d_{c\ (diff.)}$ (m)	Re_p (−)
1	0.343	15.53	–	–	–	0.07	–	2	–	1.74
2	0.343	8.47	–	–	–	0.07	–	2	–	1.74
3	0.343	5.62	–	–	–	0.07	–	2	–	1.74
4	0.343	15.53	–	–	–	0.07	–	2	–	1.74
5	0.289	15.53	–	–	–	0.07	–	2	–	1.47
6	0.289	8.47	–	–	–	0.07	–	2	–	1.47
7	0.289	5.62	–	–	–	0.07	–	2	–	1.47
8	0.289	15.53	–	–	–	0.07	–	2	–	1.47
9	0.343	15.53	134.90	–	–	0.07	–	2	–	1.74
10	0.343	15.53	10.73	4.40E-04	0.00116	0.07	1.016	2	0.13	1.74
11	0.343	8.47	8.22	3.59E-03	0.00947	0.07	8.283	2	0.02	1.74
12	0.343	5.62	4.13	1.97E-04	0.00052	0.07	0.455	2	0.29	1.74
13	0.289	15.53	–	–	–	0.07	–	2	–	1.47

(*Continued*)

Table 8. (Continued)

$a_v = 78.947\ m^{-1}$										
Case	U_g (m/s)	$k_{reaction}$ (s^{-1})	K at $H_5 = 0.267$ m (s^{-1})	$k_{mass\ transfer}$ (m/s)	Sh_p (−)	d_c (m)	Sh_c (−)	$Sh_{diff.\ limit}$ (−)	$d_{c\ (diff.)}$ (m)	Re_p (−)
1	0.343	15.53	23.19	–	–	0.07	–	2	–	1.74
2	0.343	8.47	18.06	–	–	0.07	–	2	–	1.74
3	0.343	5.62	11.95	–	–	0.07	–	2	–	1.74
4	0.343	15.53	9.06	2.76E-04	0.00073	0.07	0.636	2	0.21	1.74
5	0.289	15.53	112.70	–	–	0.07	–	2	–	1.47
6	0.289	8.47	135.62	–	–	0.07	–	2	–	1.47
7	0.289	5.62	21.89	–	–	0.07	–	2	–	1.47
8	0.289	15.53	340.37	–	–	0.07	–	2	–	1.47
9	0.343	15.53	85.36	–	–	0.07	–	2	–	1.74
10	0.343	15.53	54.69	–	–	0.07	–	2	–	1.74
11	0.343	8.47	175.17	–	–	0.07	–	2	–	1.74
12	0.343	5.62	75.09	–	–	0.07	–	2	–	1.74
13	0.289	15.53	322.06	–	–	0.07	–	2	–	1.47
Case	U_g (m/s)	$k_{reaction}$ (s^{-1})	K at $H_6 = 0.381$ m (s^{-1})	$k_{mass\ transfer}$ (m/s)	Sh_p (−)	d_c (m)	Sh_c (−)	$Sh_{diff.\ limit}$ (−)	$d_{c\ (diff.)}$ (m)	Re_p (−)
1	0.343	15.53	116.38	–	–	0.07	–	2	–	1.74
2	0.343	8.47	96.00	–	–	0.07	–	2	–	1.74
3	0.343	5.62	–	–	–	0.07	–	2	–	1.74
4	0.343	15.53	62.51	–	–	0.07	–	2	–	1.74
5	0.289	15.53	–	–	–	0.07	–	2	–	1.47
6	0.289	8.47	122.31	–	–	0.07	–	2	–	1.47
7	0.289	5.62	86.31	–	–	0.07	–	2	–	1.47
8	0.289	15.53	178.57	–	–	0.07	–	2	–	1.47
9	0.343	15.53	92.22	–	–	0.07	–	2	–	1.74
10	0.343	15.53	24.74	–	–	0.07	–	2	–	1.74
11	0.343	8.47	25.27	–	–	0.07	–	2	–	1.74
12	0.343	5.62	43.84	–	–	0.07	–	2	–	1.74
13	0.289	15.53	5.79	1.17E-04	0.00031	0.07	0.270	2	0.49	1.47

For small particles, the formation of particle clusters during experiments and computation increases the mass transfer resistance due to restricted movement of gas into the dense clusters, thus, significantly decreasing the mass transfer coefficient and Sherwood number. The conventional definition of Sherwood number considers only the difference between the bulk and surface concentrations or the radial distribution of concentration caused by hydrodynamics in fluidized beds, and not by diffusional resistance between bulk and particle surface. The diffusion mass transfer resistance becomes significant for small particles due to formation of clusters. This leads to low Sherwood number. This shows that the ratio of convection to diffusion for small particles with high tendency to form clusters is lower than that for the large particles with low tendency to form clusters. Thus, the definition of the Sherwood number for small particles is misdirecting, as it only shows a direct relation with the particle size, and not with cluster. In view of the fact that the measured and computed overall effective rate constants were close to the reaction rate constants in this study, the mass transfer was reasonably good, hence, showing that the mass transfer was not as bad as shown by extremely low values of Sherwood numbers. From the CFD simulations, the average size of the bubble or cluster was of the order of 0.07 m. Table 8 shows that the substitution of cluster or bubble size in Eq. 13 gave the Sherwood numbers for clusters or bubbles three orders of magnitude higher than those for the particles. Table 8 also summarizes the cluster or bubble sizes for the diffusion limit of two for the Sherwood number.

In summary, this paper successfully measured the low mass transfer coefficients and Sherwood numbers in fluidized beds. It was also shown that the kinetic theory based CFD codes, such as the IIT CFD code fully described in Gidaspow and Jiradilok,[39] the commercial code, FLUENT and publicly available MFIX code developed at the National Energy Technology Laboratory (NETL), Department of Energy (DOE), are capable of successfully computing the mass transfer coefficients required for fluidized bed reactor designs, without using such parameters as inputs. This eliminates the need of Kunii and Levenspiel's approximations[56] for the use of mass transfer coefficients in fluidized beds, with bubble properties as input in the models.

Conclusions

- The mass transfer coefficients and Sherwood numbers for FCC particles, impregnated with ferric nitrate, were measured and computed in the riser section of the IIT 2-D CFB, which was operated as a bubbling fluidized bed, using the first order ozone decomposition reaction.
- The effective rate constants measured from species conservation equation, using ozone and solids concentrations at various axial levels, were higher in the free board region

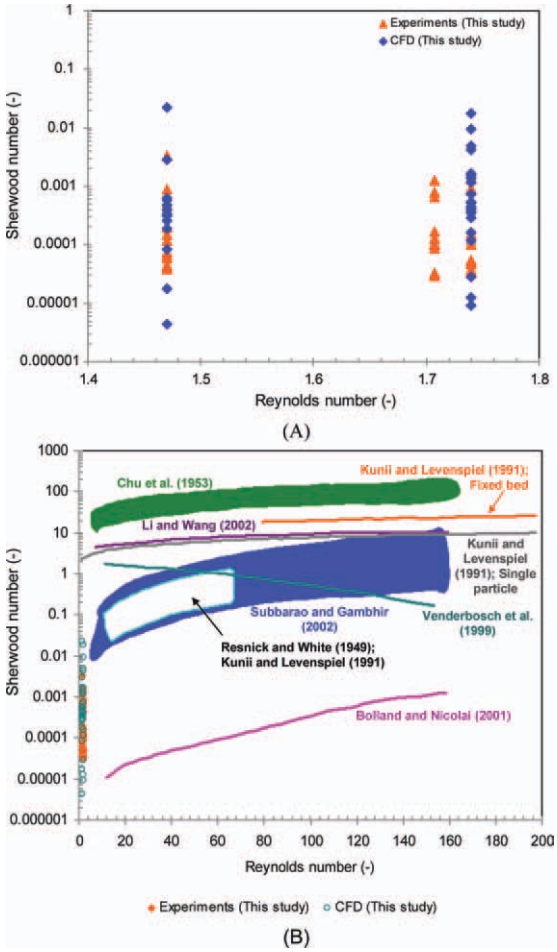

Figure 16. Comparison of measured and computed particle Sherwood number vs. particle Reynolds number data (A) in this study, and (B) with the literature values.[4,54–59]

[Color figure can be viewed in the online issue, which is available at wileyonlinelibrary.com.]

than in the bubbling region. The measured reaction rate constants were 15.53, 8.47, and 5.62 s^{-1}.

- The CFD simulations were performed using a kinetic theory based model in FLUENT, with EMMS drag, by changing the (1) superficial gas velocity; (2) reaction rate constant; (3) mesh/grid sizes; (4) initial particle bed height; and (5) geometry between three- and two-dimensions.
- The computed solids volume fraction contours showed coexistence of clusters and bubbles. The axial profiles of the solids volume fractions showed transition from bubbling to free board region at a height of around 0.15 m.
- The measured and computed ozone concentrations decreased upon moving up in the bubbling fluidized bed due to sequential decomposition of ozone on the surface of catalyzed particles, but the ozone was not completely decomposed due to the shallow bed of FCC particles. The concentration became constant in the free board region. The 3-D simulations with 100,000 fine mesh/grids reasonably matched the measured ozone concentrations, but their differences with the 3-D simulations with 35,000 relatively coarser meshes/grids and 2-D simulations were inappreciable, considering the computational time required with 3-D simulations with extremely fine grids. The ozone concentrations were higher at the center than near the walls, in the dense region, due to core-annular regime for solids volume fractions.
- The effective rate constants were computed by solving the conservation of species equation between pairs of consecutive points along the axial direction. The mass transfer coefficients and Sherwood numbers measured and computed at various axial levels inside the reactor, using the concept of additive resistances, were of the orders of 10^{-6}–10^{-3} m/s and 10^{-6}–10^{-2}, respectively. Although the computed and measured Sherwood numbers for fine particles were much lower than the diffusion limit of two, their values at low Reynolds numbers showed a reasonably good agreement with the literature values summarized by Breault,[6] especially with those obtained by extrapolating the data by Bolland and Nicolai.[4] The mass transfer coefficients and Sherwood numbers were local quantities, which changed with position within the reactor. This supports the reasoning by Breault[6] that the mass transfer coefficients and Sherwood numbers vary due to different flow regimes and locations of data acquisition in the fluidized beds.
- The formation of particle clusters in the bubbling fluidized bed increased mass transfer resistance due to the restricted movement of gas into dense clusters. The conventional definition of Sherwood number in fluidized beds considers only the difference between the bulk and surface concentrations or the radial distribution of concentration caused by hydrodynamics, and not by diffusional resistance between bulk and particle surface. In view of the fact that small particles form clusters, the diffusion mass transfer resistance becomes significant. This leads to low Sherwood number, which is defined as the ratio of convective to diffusion mass transport. This shows that the ratio of convection to diffusion for small particles with high tendency for form clusters is lower than that for large particles with low tendency to form clusters. Hence, the definition of the Sherwood number for small particles is deceiving, as it only shows a direct relation with the particle size, and not with cluster. In view of the fact that the measured and computed overall effective rate constants were close to the reaction rate constants in this study, the mass transfer was reasonably good, thus, showing that the mass transfer was not as bad as shown by extremely low values of Sherwood numbers. It was shown in this study that the Sherwood number increased by three orders of magnitude upon substituting the cluster or bubble size into the Sherwood number equation for particles.
- It was also shown that the kinetic theory based CFD codes, such as the IIT CFD code fully described in Gidaspow and Jiradilok,[39] the commercial code, FLUENT and publicly available MFIX code developed at the National Energy Technology Laboratory (NETL), Department of Energy (DOE), can successfully compute the mass transfer coefficients required for fluidized bed reactor designs, without using such parameters as inputs. This eliminates the use of Kunii and Levenspiel's approximations[56] for the mass transfer coefficients in fluidized beds, with bubble properties as an input in the models.

Acknowledgments

The authors thank the U.S. Department of Energy (DOE) University Grant (DE-FG26-06NT42736) for the financial support. They also thank Dr. Ronald Breault of DOE for the technical discussions regarding the project.

Notation

c_p = heat capacity at constant pressure (J/kg-K)
C_d = drag coefficient (-)
C_{O_3} = ozone concentration (kgmol/m^3)
d_b = diameter of bubbles (m)
$d_{b(diff.)}$ = diameter of bubbles, for $Sh_{diff.limit} = 2$ (m)
d_c = diameter of clusters (m)
$d_{c(diff.)}$ = diameter of clusters, for $Sh_{diff.limit} = 2$ (m)
e = particle–particle restitution coefficient (-)
e_w = particle-wall restitution coefficient (-)
h = specific enthalpy (J/kg)
H = riser height (m)
$k_{mass\ transfer}$ = mass transfer coefficient (m/s)
$k_{reaction}$ = reaction rate constant (s^{-1})
K = effective rate constant (s^{-1})
P = pressure (N/m^2)
Q_{gs} = intensity of heat exchange from gas phase to solid phase (J/m^3-s)
Q_{sg} = intensity of heat exchange from solid phase to gas phase (J/m^3-s)
r = radial distance from center (m)
r_i = rate of reaction of specie, i (kgmol/m^3-s)
r_{O_3} = rate of reaction (kgmol/m^3-s)
S = source term due to chemical reaction (J/m^3-s)
Sh = Sherwood number (-)
$Sh_{diff.limit}$ = Sherwood number with diffusional limit of 2 (-)
t = time interval (s)
v_g = gas velocity (m/s)
$v_{s,slip}$ = slip velocity at wall (m/s)

Greek letters

β_A = gas-solid drag coefficient for Hydrodynamic model A (kg/m^3-s)
ε_g = gas volume fraction or voidage (-)
ε_s = solids volume fraction (-)
$\varepsilon_{s,bubbling\ bed}$ = solids volume fraction in bubbling region (-)
$\varepsilon_{s,max.}$ = maximum solids volume fraction or packing fraction (-)
μ_g = viscosity of air (kg/m-s)
μ_s = solids shear viscosity (kg/m-s)
ρ = density of the material (kg/m^3)
$\tau_{ph.}$ = stress tensor for phase ph (Pa)
θ = granular temperature (m^2/s^2)

Subscripts

0,1…7 = axial position
g = gas phase
ph. = phase
s = solid phase

Literature Cited

1. Gunn DJ. Transfer of heat or mass to particles in fixed and fluidized beds. *Int J Heat Mass Transfer*. 1978;21:467–476.
2. Kato K, Kubota H, Wen CY. Mass transfer in fixed and fluidized beds. *Chem Eng Progr Symp Series*. 1970;105:87–99.
3. Zabrodsky SS. *Hydrodynamics and Heat Transfer in Fluidized Beds*. Cambridge: MIT Press, 1966.
4. Bolland O, Nicolai R. Describing mass transfer in circulating fluidized beds by ozone decomposition. *Chem Eng Commun*. 2001;187:1–21.
5. Chalermsinsuwan B, Piumsomboon P, Gidaspow D. Kinetic theory based computation of PSRI riser: Part II—computation of mass transfer coefficient with chemical reaction. *Chem Eng Sci*. 2009;64:1212–1222.
6. Breault RW. A review of gas–solid dispersion and mass transfer coefficient correlations in circulating fluidized beds. *Powder Technol*. 2006;163:9–17.
7. Breault RW, Guenther CP. Mass transfer in the core-annular and fast fluidization flow regimes of a CFB. *Powder Technol*. 2009;190:385–389.
8. Chalermsinsuwan B, Piumsomboon P, Gidaspow D. Kinetic theory based computation of PSRI riser: Part I—estimation of mass transfer coefficient. *Chem Eng Sci*. 2009;64:1195–1211.
9. Fryer C, Potter OE. Experimental investigation of models for fluidized bed catalytic reactors. *AIChE J*. 1976;22:38–47.
10. Ouyang S, Lin J, Potter OE. Ozone decomposition in a 0.254 m diameter circulating fluidized bed reactor. *Powder Technol*. 1993;75:73–78.
11. Ouyang S, Lin J, Potter OE. Circulating fluidized bed as a catalytic reactor: experimental study. *AIChE J*. 1995;41:1534–1542.
12. Samuelsberg A, Hjertager BH. *Simulation of two-phase gas/particle flow and ozone decomposition in a 0.25 m I.D. Riser*. In: Serizawa A, Fukano T, Batalille J, editors. *Advances in Multiphase Flow*. Amsterdam: Elsevier, 1995:679–688.
13. Syamlal M, O'Brien TJ. Fluid dynamic simulation of O_3 decomposition in a bubbling fluidized bed. *AIChE J*. 2003;49:2793–2801.
14. Therdthianwong A, Pantaraks P, Therdthianwong S. Modeling and simulation of circulating fluidized bed reactor with catalytic ozone decomposition reaction. *Powder Technol*. 2003;133:1–14.
15. Hansen KG, Solberg T, Hjertager BH. A three-dimensional simulation of gas/particle flow and ozone decomposition in the riser of a circulating fluidized bed. *Chem Eng Sci*. 2004;59:5217–5224.
16. Fan C, Zhang Y, Bi X, Song W, Lin W, Luo L. Evaluation of downer reactor performance by catalytic ozone decomposition. *Chem Eng J*. 2008;140:539–554.
17. van der Vaart DR. Prediction of axial concentration profiles in catalytic fluidized reactors. *AIChE J*. 1992;38:1157–1160.
18. Schoenfelder H, Kyuse M, Werther J. Two-dimensional model for circulating fluidized bed reactors. *AIChE J*. 1996;42:1875–1888.
19. Dong W, Wang W, Li J. A multiscale mass transfer model for gas-solid riser flows: Part 1-Sub-grid model and simple tests. *Chem Eng Sci*. 2008;63:2798–2810.
20. Kashyap M, Gidaspow D. Computation and measurements of mass transfer and dispersion coefficients in fluidized beds. *Powder Technol*. 2010;203:40–56.
21. Frye CG, Lake WC, Eckstrom HC. Gas-solid contacting with ozone decomposition reaction. *AIChE J*. 1958;4:403–408.
22. Jiang P, Bi H, Jean R, Fan L. Baffle effects on performance of catalytic circulating fluidized bed reactor. *AIChE J*. 1991;37:1392–1400.
23. Pagliolico S, Tiprigan M, Rovero G, Gianetto A. Pseudo-homogeneous approach to CFB reactor design. *Chem Eng Sci*. 1992;47:2269–2274.
24. Dhandapani B, Oyama ST. Gas phase ozone decomposition catalysts. *Appl Catal B*. 1997;11:129–166.
25. Gidaspow D. *Multiphase Flow and Fluidization: Continuum and Kinetic Theory Descriptions*. New York: Academic Press, 1994.
26. Driscoll MC. A study of the fluidization of FCC particles and nanoparticles in a rectangular bed and a riser. Ph.D. Thesis, Illinois Institute of Technology, Chicago, Illinois, 2007.
27. Driscoll MC, Gidaspow D. Wave propagation and granular temperature in fluidized beds of nanoparticles. *AIChE J*. 2007;53:1718–1726.
28. Kashyap M, Gidaspow D, Driscoll M. Effect of electric field on the hydrodynamics of fluidized nanoparticles. *Powder Technol*. 2008;183:441–453.
29. Kashyap M. Measurements and computation of dispersion and mass transfer coefficients in fluidized beds. Ph.D. Thesis, Illinois Institute of Technology, Chicago, Illinois, 2010.
30. Seo YC, Gidaspow D. An x-ray-γ-ray method of measurement of binary solids concentrations and voids in fluidized beds. *Ind. Eng. Chem. Res*. 1987;26:1622–1628.
31. Fogler HS. *Elements of Chemical Reaction Engineering*. New Jersey: Prentice-Hall, 1999.
32. Levenspiel O. *Chemical Reaction Engineering*. New York: Wiley, 1999.
33. van Swaaij WPM, Zuiderweg FJ. *Investigation of ozone decomposition in fluidized beds on the basis of a two-phase model. Proceedings of the European Symposium on Chemical Engineering*. Amsterdam: Elsevier, October 1-5, 1973:B9.25-B9.36.
34. Solbrig CW, Gidaspow D. Convective diffusion in a parallel plate duct with one catalytic wall-laminar flow-first order reaction. Part I-analytical. *Can J Chem Eng*. 1967;45:35–39.
35. Kulacki FA, Gidaspow D. Convective diffusion in a parallel plate duct with one catalytic wall-laminar flow-first order reaction. Part II-experimental. *Can J Chem Eng*. 1967;45:72–78.
36. Bird RB, Stewart WE, Lightfoot EN. *Transport Phenomena*. New York: Wiley, 2002.
37. Kashyap M, Gidaspow D. Circulation of Geldart D type particles: Part II—low solids fluxes. Measurements and computation under dilute conditions. *Chem Eng Sci*. 2011;66:1649–1670.
38. Kashyap M, Gidaspow D, Koves WJ. Circulation of Geldart D type particles: Part I—high solids fluxes. Measurements and computation under solids slugging conditions. *Chem Eng Sci*. 2011;66:183–206.

39. Gidaspow D, Jiradilok V. *Computational Techniques: The Multiphase CFD Approach to Fluidization and Green Energy Technologies (Includes CD-ROM)*. New York: Nova Science Publishers, 2009.
40. Fluent Inc. *Fluent 6.2 User's Guide*. New Hampshire: Fluent, 2005.
41. Xie N, Battaglia F, Pannala S. Effects of using two- versus three-dimensional computational modeling of fluidized beds. Part I, hydrodynamics. *Powder Technol*. 2008;182:1–13.
42. Ding J, Gidaspow D. A bubbling fluidization model using kinetic theory of granular flow. *AIChE J*. 1990;36:523–538.
43. Neri A, Gidaspow D. Riser hydrodynamics: simulation using kinetic theory. *AIChE J*. 2000;46:52–67.
44. Fluent Inc. *Fluent 6.2 UDF Manual*. New Hampshire: Fluent, 2005.
45. Yang N, Wang W, Ge W, Li J. CFD simulation of concurrent-up gas–solid flow in circulating fluidized beds with structure-dependent drag coefficient. *Chem Eng J*. 2003;96:71–80.
46. Yang N, Wang W, Ge W, Wang L, Li J. Simulation of heterogeneous structure in a circulating fluidized-bed riser by combining the two-fluid model with the EMMS approach. *Ind Eng. Chem Res*. 2004;43:5548–5561.
47. Wen CY, Yu YH. Mechanics of fluidization. *Chem Eng Prog Symp Series*. 1966;62:100–111.
48. Johnson PC, Jackson R. Frictional-collisional constitutive relations for granular materials, with application to plane shearing. *J Fluid Mech*. 1987;176:67–93.
49. Gelderbloom S, Gidaspow D, Lyczkowski RW. CFD simulations of bubbling /collapsing fluidized beds for three Geldart groups. *AIChE J*. 2003;49:844–858.
50. van Wachem BGM, Schouten JC, van den Bleek CM, Krishna R, Sinclair JL. Comparative analysis of CFD models of dense gas–solid systems. *AIChE J*. 2001;47:1035–1051.
51. McKeen T, Pugsley T. Simulation and experimental validation of a freely bubbling bed of FCC catalyst. *Powder Technol*. 2003;129:139–152.
52. Weinstein H, Meller M, Shao MJ, Parisi RJ. Radial solid density variation in a fast fluidized bed. *AIChE Symp. Series*. 1984;80:52–59.
53. Hartge EU, Rensner D, Werther J. *Solids concentration and velocity patterns in circulating fluidized beds*. In Basu P, Large JF, editors. *Circulating Fluidized Bed Technology II*. Oxford: Pergamon Press, 1988:165–170.
54. Resnick W, White RR. Mass transfer in systems of gas and fluidized solids. *Chem Eng Prog*. 1949;45:377–390.
55. Chu JC, Kalil J, Wetteroth WA. Mass transfer in a fluidized bed. *Chem Eng Prog*. 1953;49:141–149.
56. Kunii D, Levenspiel O. *Fluidization Engineering*, 2nd ed. Boston: Butterworth-Heinemann, 1991.
57. Venderbosch RH, Prins W, van Swaaij WPM. Mass transfer and influence of the local catalyst activity on the conversion in a riser reactor. *Can J Chem Eng*. 1999;77:262–274.
58. Li J, Wang L. *Concentration distributions during mass transfer in circulating fluidized beds*. Presented at the Seventh International Conference on Circulating Fluidized Beds. Niagara Falls, Ontario, Canada, May 5–8, 2002.
59. Subbarao D, Gambhir S. *Gas particle mass transfer in risers*. Presented at the Seventh International Conference on Circulating Fluidized Beds. Niagara Falls, Ontario, Canada, May 5–8, 2002.

Appendix: An Example of the Measurement of Mass Transfer Coefficient and Sherwood Number

In Table 4, Row 1 shows the results for Case C, with $U_g = 0.289$ m/s. Use data at $Y_0 = 0$ m and $Y_1 = 0.076$ m. Ozone concentrations were, $C_{O_3(\text{inlet})} = 10.5$ PPM and $C_{O_3(1)} = 6.36$ PPM. Solids volume fractions were, $\varepsilon_{s_0} = 0.66$ and $\varepsilon_{s_1} = 0.618$.

Using Eq. 14,

$$0.289\frac{(6.36-10.5)}{(0.076-0)} = -K\frac{(6.36+10.5)}{2}\frac{(0.618+0.66)}{2} \tag{A1}$$

Therefore, $K = 2.91\text{s}^{-1}$.

The reaction rate constant obtained by solving linear equations for effective rate constant vs. superficial gas velocity, at the heights of 0.711 and 0.381 m, was $k_{\text{reaction}} = 15.53\text{s}^{-1}$.

The surface area per unit volume of a spherical particle was, $a_v = \frac{6}{d_p} = \frac{6}{7.6\times10^{-6}} = 78,947\text{m}^{-1}$.

By using Eq. 12,

$$\frac{1}{2.91} = \frac{1}{k_{\text{mass transfer}}\times 78,947} + \frac{1}{15.53} \tag{A2}$$
$$k_{\text{mass transfer}} = 4.54\times10^{-5}\text{m/s}.$$

By using Eq. 13,

$$Sh = \frac{4.54\times10^{-5}\times76\times10^{-6}}{2.88\times10^{-5}} = 0.00012 \tag{A3}$$

The size of the largest bubble was, $d_{\text{bubble}} = 0.11$ m.

The Sherwood number based on the largest bubble was,

$$Sh_b = \frac{0.00012\times0.11}{76\times10^{-6}} = 0.174 \tag{A4}$$

Manuscript received Jun. 17, 2010, revision received Nov. 3, 2010, and final revision received Mar. 10, 2011.